CELLULAR NEUROSCIENCE

Molecular self-avoidance in synaptic neurexin complexes

Cosmos Yuqi Wang[1]*, Justin H. Trotter[1], Kif Liakath-Ali[1], Sung-Jin Lee[1], Xinran Liu[2], Thomas C. Südhof[1,3]*

Synapses are thought to be organized by interactions of presynaptic neurexins with postsynaptic ligands, particularly with neuroligins and cerebellins. However, when a neuron forms adjacent pre- and postsynaptic specializations, as in dendrodendritic or axo-axonic synapses, nonfunctional cis neurexin/ligand interactions would be energetically favored. Here, we reveal an organizational principle for preventing synaptic cis interactions ("self-avoidance"). Using dendrodendritic synapses between mitral and granule cells in the olfactory bulb as a paradigm, we show that, owing to its higher binding affinity, cerebellin-1 blocks the cis interaction of neurexins with neuroligins, thereby enabling trans neurexin/neuroligin interaction. In mitral cells, ablating either cerebellin-1 or neuroligins severely impaired granule cell→mitral cell synapses, as did overexpression of wild-type neurexins but not of mutant neurexins unable to bind to neuroligins. Our data uncover a molecular interaction network that organizes the self-avoidance of nonfunctional neurexin/ligand cis interactions, thus allowing assembly of physiological trans interactions.

INTRODUCTION

Neural circuits are constructed by synaptic connections that link neurons into communicating networks. During development and throughout life, synapse formation is organized by heterophilic adhesion molecules that initiate the establishment of synapses and shape their properties and plasticity (*1*–*5*). Among many synaptic adhesion molecules that were described, presynaptic neurexins stand out because they regulate the properties of most synapses (*6*) and because loss of function mutations in neurexins are repeatedly observed in neuropsychiatric disorders (*7*–*9*).

In connecting neurons into neural circuits, synapses exhibit a vast range of molecular and functional architectures that are shaped, at least, in part, by neurexins (*6*). A prototypical synapse is formed by a presynaptic axonal bouton contacting a postsynaptic dendrite. A subset of synapses, however, does not conform to this standard design. Among nonstandard synapses, reciprocal dendrodendritic synapses are remarkable because they comprise antiparallel synaptic junctions formed by neighboring dendrites (Fig. 1A) (*10*). Both two dendrites generate pre- and postsynaptic specializations, thereby assembling a two-neuron microcircuit, the smallest possible neural circuit. Similarly, at axo-axonic synapses formed by inhibitory neurons onto presynaptic terminals, an axonal membrane assembles both pre- and postsynaptic specializations (*11*, *12*). In these synapses, pre- and postsynaptic specializations are adjacent to each other in the same plasma membrane domain.

Reciprocal dendrodendritic synapses between mitral/tufted cells and granule cells in the olfactory bulb (OB) constitute its most abundant synapses (*13*, *14*). Reciprocal mitral-granule cell synapses are essential for olfactory information processing (*15*) and are modulated by synaptic plasticity that mediates olfactory learning (*16*). Moreover, reciprocal dendrodendritic synapses are not restricted to the OB but widely distributed in brain. They are, among others, abundant in the lateral geniculate nucleus (*17*), the ventro-lateral nucleus of the thalamus (*18*), the motor cortex (*19*), and the retina (*20*). The organization of reciprocal dendrodendritic and axo-axonic synapses poses a unique cell biological problem because of the lack of spatial segregation between their adjacent pre- and postsynaptic specializations (Fig. 1, A and B). Although synapses are largely organized by trans-synaptic adhesion molecules, such molecules are present in the same plasma membrane next to each other in dendrodendritic and axo-axonic synapses. Thus, a self-avoidance mechanism must exist that prevents heterophilic adhesion molecules from engaging in energetically favored cis complexes. However, no such mechanism has been described.

Neurexins organize synapses by interacting with multiple postsynaptic ligands, including Nlgns, Cblns, that, in turn, bind to GluD1/2 (the delta subfamily of glutamate receptors) or to DCC (Deleted in Colorectal Cancer)/neogenin, LRRTMs (Leucine-rich repeat transmembrane neuronal proteins, and dystroglycan (*6*, *21*–*23*). In vertebrates, neurexins are encoded by three genes (*Nrxn1-3* in mice) that express two principal forms, longer α-neurexins and shorter β-neurexins. α-Neurexins and β-neurexins are transcribed from distinct promoters and are extensively alternatively spliced (*24*–*26*). In addition, the *Nrxn1* gene has a third promoter for an even shorter γ-isoform (Nrxn1γ) (*27*). Neurexins are highly expressed in all neurons but at different levels for each isoform (*28*, *29*). Neurexins perform distinct essential functions in different synapses, ranging from controlling the presynaptic release probability to regulating the postsynaptic receptor composition. Their diverse functions are likely based on their molecular diversity and their multifarious ligand interactions, which together create a neurexin code (*6*).

Trans-synaptic signaling by presynaptic neurexins that engage postsynaptic ligands is conceptually straightforward in standard synapses. In dendrodendritic and axo-axonic synapses, however, adjacent pre- and postsynaptic specializations contain neurexins and neurexin ligands, favoring cis interactions. Thus, the question arises how adjacent pre- and postsynaptic specializations in dendrodendritic and axo-axonic synapses achieve self-avoidance—how are synaptic

[1]Department of Molecular and Cellular Physiology, School of Medicine, Stanford University, Stanford, CA 94305, USA. [2]Department of Cell Biology, School of Medicine, Yale University, New Haven, CT 06510, USA. [3]Howard Hughes Medical Institute, School of Medicine, Stanford University, Stanford, CA 94305, USA.
*Corresponding author. Email: cosmosyw@stanford.edu (C.Y.W.); tcs1@stanford.edu (T.C.S.)

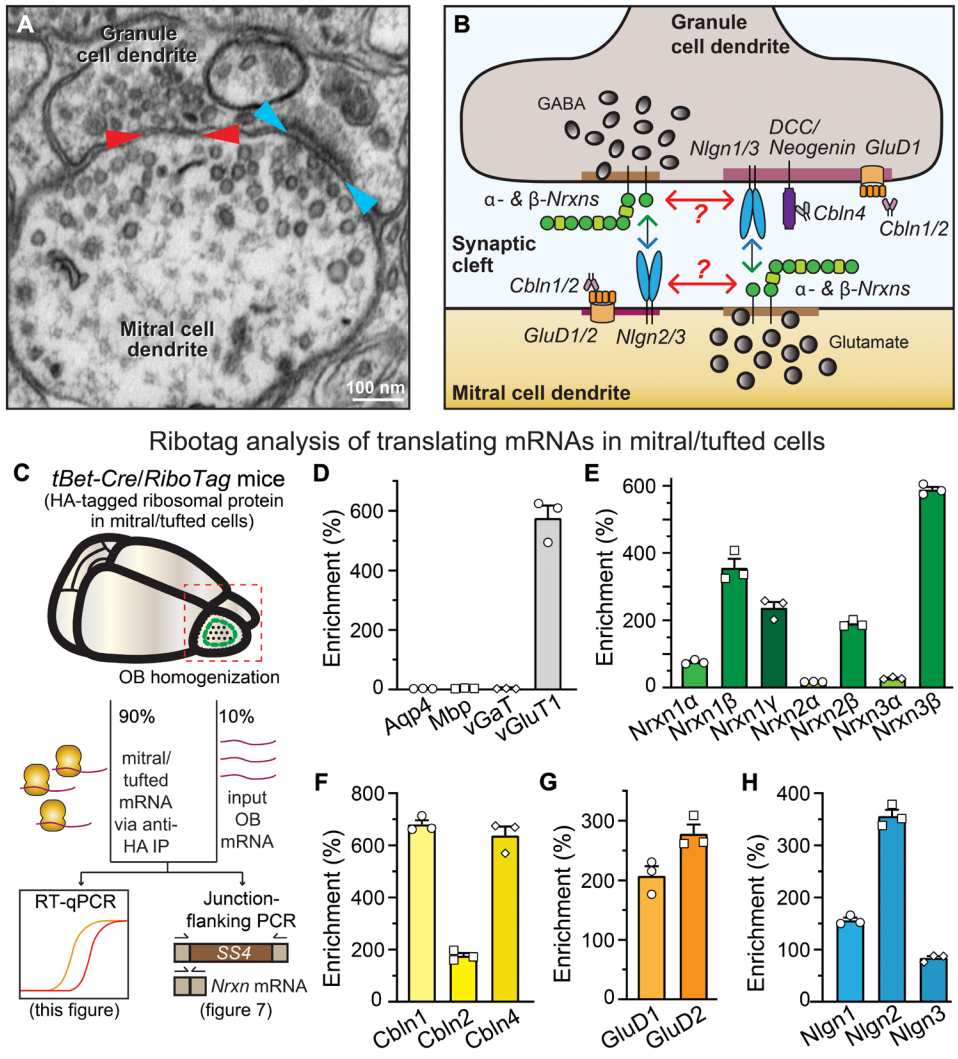

Fig. 1. Mitral cells that form reciprocal dendrodendritic synapses coexpress neurexins and multiple neurexin ligands. (**A**) Representative electron microscopy (EM) image of a reciprocal synapse in the OB (red arrowheads, inhibitory GC➔MC synapse; cyan arrowheads, excitatory mitral cell➔granule cell synapse). (**B**) Schematic of trans and cis interactions of neurexin-based synaptic adhesion molecules. Neurexins and their ligands are coexpressed in both mitral and granule cells. Because of the lack of physical compartmentalization, neurexins may interact with their ligands both in cis and trans configurations, with cis interactions potentially inhibiting trans interactions. The question of how two antiparallel neurexin signaling processes are organized to enable trans over cis interactions underlies the key to understanding the design principle of reciprocal synapses. Note that, in the diagram, the assignment of the pre- versus postsynaptic localization of various neurexin ligands is for illustration purposes, and all ligands might actually be on both sides. (**C**) Experimental strategy to isolate translating mRNAs from mitral and tufted cells using RiboTag mice and for analysis of these mRNAs. (**D**) Summary graph demonstrating that mitral and tufted cell–specific mRNAs are de-enriched in mRNAs encoding aquaporin-4 (Aqp4, astrocyte marker), myelin basic protein (Mbp, oligodendrocyte marker), and vGaT (inhibitory neuron marker) but highly enriched in vGluT1 (excitatory neuron marker). (**E** to **H**) Summary graph demonstrating that mitral and tufted cells coexpress specific isoform of neurexins (E), cerebellins (F), GluD1 and GluD2 (G), and neuroligins (H). All numerical data are means ± SEM ($n = 3$ mice).

adhesion complexes organized to prevent cis interactions and favor trans interactions?

To address this fundamental cell biological question, we here studied neurexin-based cis and trans complexes in reciprocal dendrodendritic synapses in the OB. Unexpectedly, we find that two neurexin ligands, neuroligins and Cbln1, are both required in mitral cells postsynaptically for granule cell➔mitral cell (GC➔MC) synaptic transmission. We show that Cbln1 has a much higher affinity for neurexins than neuroligins, thereby enabling Cbln1 to block the cis interaction of neurexins with neuroligins and to facilitate formation of trans interactions. This mechanism mediates self-avoidance of neurexin-ligand interactions, which makes it possible to organize the two antiparallel neurexin signaling pathways in reciprocal synapses.

RESULTS

Mitral cell Cbln1 is essential for the organization of GC➔MC synapses

Mitral/tufted cells can be selectively manipulated in mice using Cre-recombinase expressed under the control of the *tBet* promoter (*30*). Crosses of *tBet-Cre* mice with *Ai14* mice in which tdTomato

expression is activated by Cre-mediated recombination (*31*) validated exclusive expression of Cre in mitral/tufted cells of the OB (Fig. 2B). Using Cre-dependent *RiboTag* mice crossed with *tBet-Cre* mice (*30*, *32*), we selectively isolated mRNAs that are translated in mitral/tufted cells (Fig. 1C). Real-time quantitative polymerase chain reaction (qPCR) showed that, as expected, mRNAs encoding the excitatory neuron marker *vGluT1* were abundant in mitral/tufted cells, whereas mRNAs encoding the astrocyte marker *Agp4*, the oligodendrocyte marker *Mbp*, or the inhibitory neuron marker *vGaT* were largely absent (Fig. 1D). Consistent with previous in situ hybridization data (*28*, *29*), mitral/tufted cells expressed high levels of β-neurexins (Fig. 1E). In contrast, α-neurexins were de-enriched (Fig. 1E). mRNAs encoding neuroligins, cerebellins, and the cerebellin receptors GluD1 and GluD2 were also abundant in mitral cells (Fig. 1, F to H). Cbln1 and Cbln4 mRNAs were highly enriched, whereas Cbln2 mRNAs were not as abundant (Fig. 1F). Cbln3 was not examined because of its exclusive expression in the cerebellum (*33*). Using single-molecule RNA in situ hybridization, we asked whether mitral and tufted cells equally synthesize various cerebellin isoforms. Cbln1 was more strongly expressed in mitral cells than in tufted cells, whereas Cbln4 exhibited the opposite pattern (Fig. 2A). Cbln2 was present at much lower levels in both mitral/tufted cells but expressed at high levels in granule and periglomerular cells (Fig. 2A).

Because of its robust expression, we examined the role of Cbln1 in dendrodendritic synapses of mitral cells. We filled patched mitral cells in acute OB slices with neurobiotin, which confirmed the typical cellular architecture of mitral cells (Fig. 2C). To generate mice with a mitral/tufted cell–specific deletion of *Cbln1*, we crossed *tBet-Cre* mice with *Cbln1* conditional knockout (cKO) mice (Fig. 2D) (*30*, *34*). The *Cbln1* deletion in mitral/tufted cells severely suppressed (~90% decrease) the total Cbln1 mRNA levels in the OB, confirming that mitral/tufted cells express the vast majority of the Cbln1 in the OB (Fig. 2E). Behavioral experiments revealed that the mitral/tufted cell–specific deletion of *Cbln1* significantly impaired a mouse's foraging behavior as assayed by the buried food test (Fig. 2G). The mitral/tufted cell deletion of *Cbln1* also decreased the sociability of mice without affecting their general mobility or anxiety levels (Fig. 2, F to H). Thus, mitral/tufted cell expression of Cbln1 is essential for olfactory behaviors.

We next examined the effect of the mitral cell *Cbln1* deletion on synaptic transmission. Whole-cell patch-clamp recordings in acute slices revealed that the *Cbln1* deletion reduced the frequency of both miniature inhibitory postsynaptic currents (mIPSCs) (~35%) and miniature excitatory postsynaptic currents (mEPSCs) (~50%) without significantly altering their amplitudes or kinetics (Fig. 2, I to N, and fig. S1, A to D). The *Cbln1* deletion did not affect the capacitance or resistance of mitral cells, suggesting that the cells were healthy (fig. S1, E and F). Thus, postsynaptic Cbln1 is required for organizing both inhibitory and excitatory inputs onto mitral cells.

The postsynaptic requirement of Cbln1 for the function of mitral cell synapses is unexpected because Cbln1 is thought to regulate excitatory and inhibitory synapse formation by a presynaptic mechanism (*35*–*39*), although we recently detected a postsynaptic action of Cbln2 in excitatory hippocampal and midbrain synapses (*40*, *41*). Because most mIPSCs in mitral cells are derived from dendrodendritic GC➔MC synapses, the decrease in mIPSC frequency suggests that Cbln1 functions in GC➔MC synapses. To test this notion, we recorded evoked IPSCs (eIPSCs) in mitral cells that were induced by stimulating the apical dendrites of granule cells (Fig. 3A). We used input/output measurements to control for the variability in the placement of the stimulating electrode. These experiments revealed that the *Cbln1* deletion caused a major decrease (~45%) in GC➔MC synaptic strength (Fig. 3, B to D). In addition, the *Cbln1* deletion increased the rise but not decay times of GC➔MC IPSCs (Fig. 3, E and F). These data are unexpected because no previous evidence implicates Cbln1 in inhibitory synaptic transmission.

Most inhibitory inputs onto mitral cells are provided by granule cells, but periglomerular neurons, short-axon cells, and other types of interneurons also form inhibitory synapses on mitral cells (*42*, *43*). To reveal whether the phenotype of the *Cbln1* deletion at inhibitory synapses is specific for GC➔MC synapses or whether it broadly applies to all inhibitory synapses of mitral cells, we measured IPSCs evoked by stimulating inhibitory periglomerular inputs (fig. S2). We detected only a small increase in synaptic strength that was not statistically significant when the slopes of input/output curves were calculated (fig. S2, C and D). Thus, the *Cbln1* deletion does not uniformly impair all inhibitory synapses of mitral cells.

Deletion of *Cbln1* decreases GABA-induced IPSCs but not GABA release

At least three mechanisms could account for the synaptic impairment induced by the *Cbln1* deletion: A decrease in the presynaptic release probability at GC➔MC synapses, a decline in postsynaptic receptor responses, or a reduction in synapse numbers. To distinguish among these three hypotheses, we examined the coefficient of variation (CV) and the paired-pulse ratio (PPR) of eIPSCs as indirect but sensitive measures of release probability (both monitored at a 75-μA stimulus intensity). The *Cbln1* deletion had no significant effect on the CV or the PPR in GC➔MC synapses (Fig. 3, G to I), suggesting that the release probability was unchanged. We confirmed this lack of presynaptic change in release probability by comparing the properties of IPSCs in control and *Cbln1*-deficient synapses as a function of the Ca^{2+} concentration in the bath solution (fig. S1, G to V). Lowering the extracellular Ca^{2+} concentration from the standard 2.5 mM to 1.0 mM Ca^{2+}, which decreases the release probability, caused no change in the effect of the *Cbln1* deletion on eIPSCs. In particular, the lack of an effect of the *Cbln1* deletion on either the CV of eIPSCs or the PPR remained the same, confirming that the *Cbln1* deletion does not significantly alter the release probability. Note that, in these experiments, the use of a different stimulating electrode produced a shift in absolute values of different parameters, while the relative changes (or lack thereof) were the same (fig. S1, G to V).

Next, we explored the possibility that the *Cbln1* deletion decreases postsynaptic γ-aminobutyric acid type A ($GABA_A$) receptor responses at GC➔MC synapses. For this purpose, we directly "puffed" GABA onto the mitral cell soma using a Picospritzer and monitored the resulting IPSCs (Fig. 3J). Notably, we observed a robust reduction (~30%) in GABA-induced IPSCs in *Cbln1*-deficient mitral cells (Fig. 3, K to M). This phenotype is consistent with the notion that the *Cbln1* deletion suppresses postsynaptic $GABA_A$ receptor responses but does not rule out a decrease in inhibitory synapse numbers, which would also decrease the overall $GABA_A$ receptor response. Note that the observed decrease in mIPSC frequency in *Cbln1*-deficient mitral cells (Fig. 2M) would also be consistent with both a lowered $GABA_A$ receptor responsiveness or a decrease in synapse numbers because a decreased GABA response

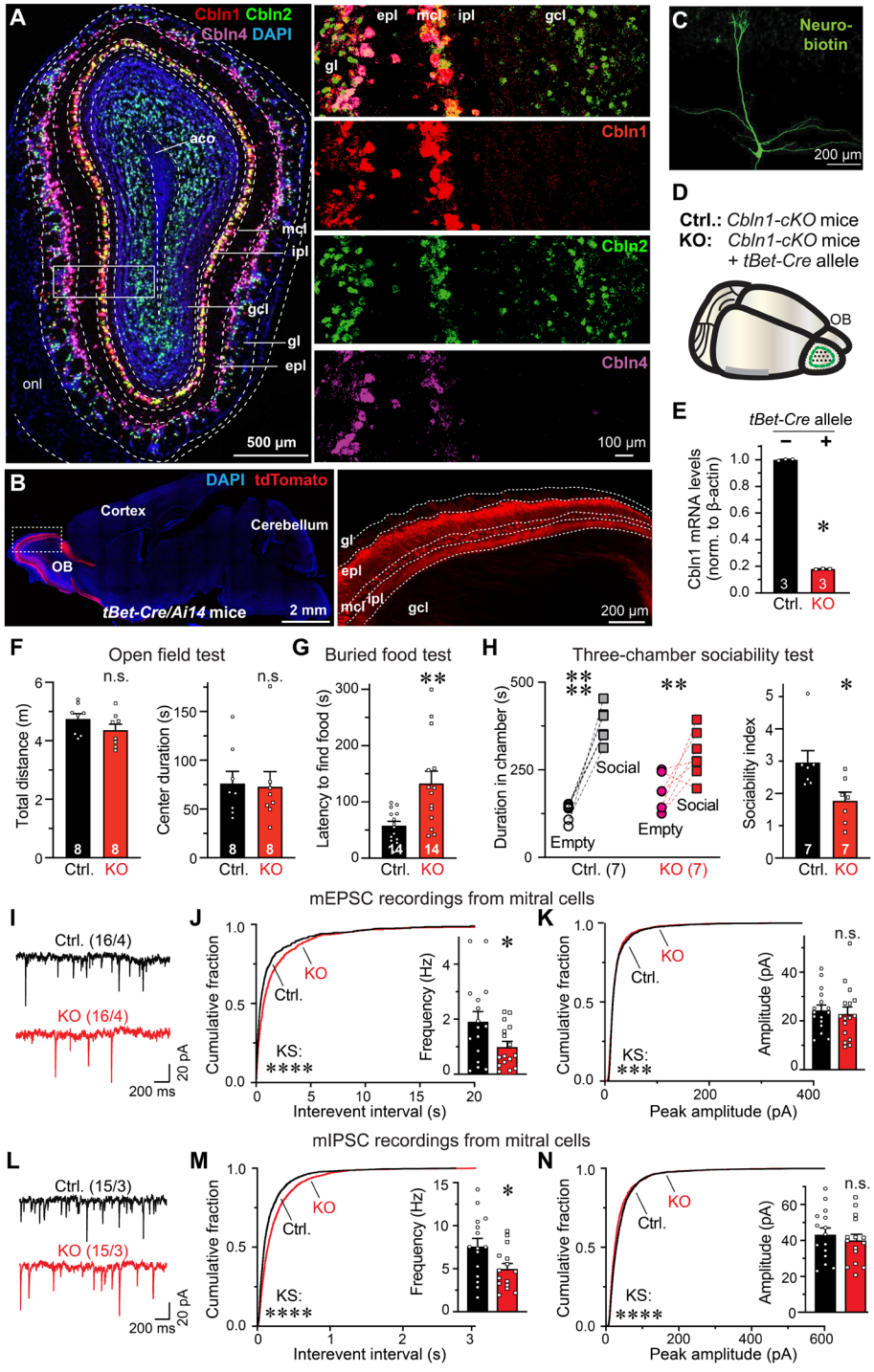

Fig. 2. Deletion of *Cbln1* from mitral/tufted cells impairs olfactory behaviors and synaptic inputs onto mitral cells. (**A**) Cbln1, Cbln2, and Cbln4 are differentially expressed in OB neurons as revealed by single-molecule in situ hybridization (left, overview; right, higher-magnification views; onl, olfactory sensory neuron layer; gl, glomerulus layer; epl, external plexiform layer; mcl: mitral cell layer; ipl, internal plexiform layer; gcl, granule cell layer; aco, anterior commissure of the olfactory limb). DAPI, 4′,6-diamidino-2-phenylindole. (**B**) Validation of mitral/tufted cell–specific Cre expression using *tBet-Cre/Ai14* mice (left, overview; right, high-magnification image of the OB). (**C**) Representative image of a neurobiotin-filled mitral cell. (**D**) Experimental strategy for the mitral/tufted cell–specific *Cbln1* deletion. (**E**) Cbln1 mRNA levels in the OB of *Cbln1* cKO/*tBet-Cre* mice (normalized to actin). (**F** to **H**) *Cbln1* deletion from mitral/tufted cells impairs olfactory behaviors [(F) open field test; (G) buried food test; (H) three-chamber sociability test]. (**I** to **N**) *Cbln1* deletion decreases the frequency of mEPSCs (I to K) and mIPSCs {(L to N); (I and L) representative traces; (J, K, M, and N) cumulative distributions of interevent intervals (J and M) or amplitudes (K and N) [insets: bar graph of the mEPSC and mIPSC frequency (J and M) or amplitudes (K and N)]}. Data are means ± SEM. Sample sizes are shown in the figures [(E to H) number of mice] or representative traces [(I and L) number of cells per mice]. Statistical significance was assessed by Kolmogorov-Smirnov (KS) tests (J, K, M, and N), Student's *t* test (E to H, J, K, M, and N), and two-way analysis of variance (ANOVA) with Bonferroni test (H, left), with $^{*}P < 0.05$, $^{**}P < 0.01$, $^{***}P < 0.001$, and $^{****}P < 0.0001$. Ctrl., control; KO, knockout; n.s., not significant.

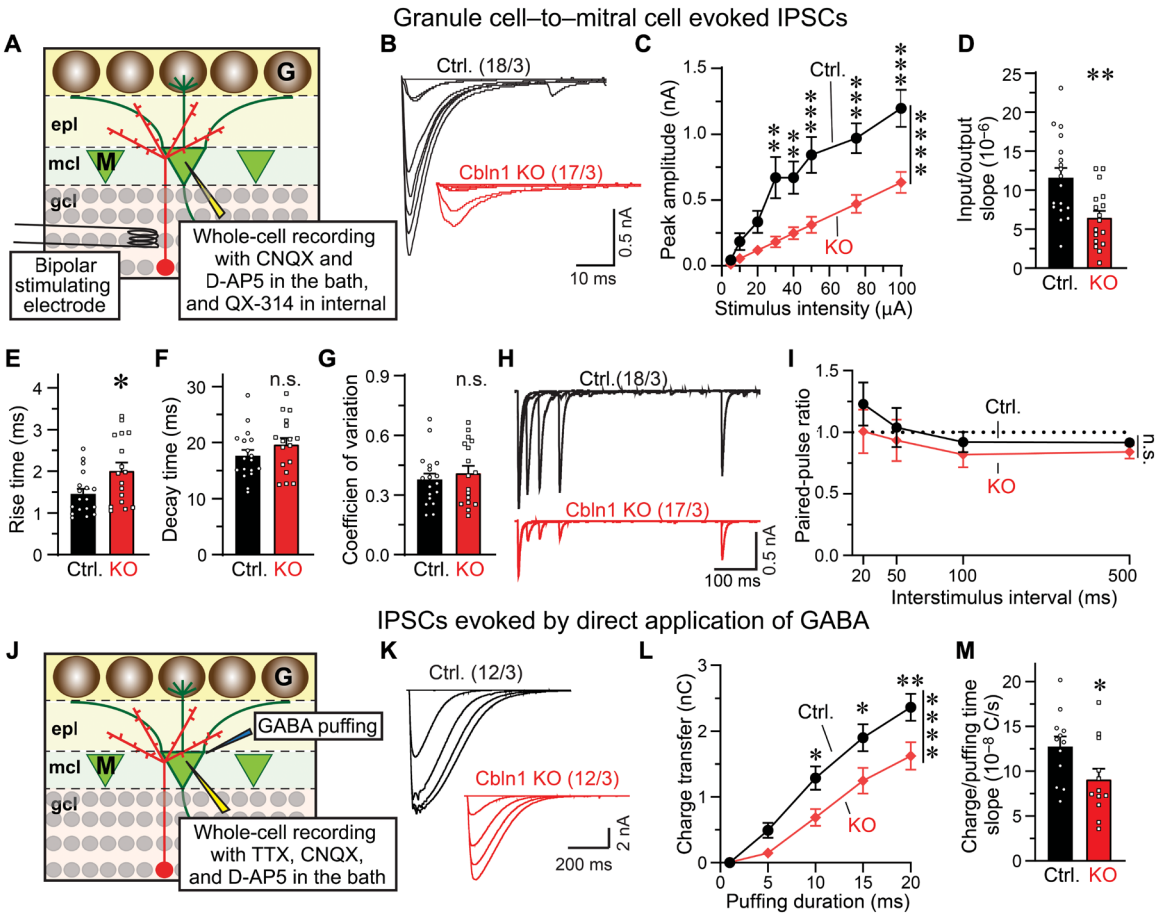

Fig. 3. Mitral cell Cbln1 enables GC➔MC synaptic transmission via a postsynaptic mechanism that regulates $GABA_A$ receptor responses. (**A**) Recording paradigm for IPSCs evoked by stimulation of granule cell dendrites with an extracellular concentric bipolar electrode. (**B** to **D**) The *Cbln1* deletion in mitral/tufted cells severely impairs GC➔MC synaptic transmission. Recordings are from acute OB slices from homozygous *Cbln1 cKO*/hemizygous *tBet-Cre* mice [(B) representative traces; (C) input/output curve of GC➔MC IPSC peak amplitudes as a function of stimulus intensity; (D) summary graph of the slopes of input/output curves]. (**E** and **F**) The *Cbln1* deletion decelerates the kinetics of GC➔MC IPSCs in mitral cells [(E) rise time; (F) decay time; both measured at a 75-μA stimulus intensity). (**G** to **I**). The *Cbln1* deletion has no effect on the coefficient of variation (CV) (G) or paired-pulse ratio (PPR) [representative traces in (H) and summary in (I)] of GC➔MC IPSCs in mitral cells (all monitored at a 75-μA stimulus intensity). (**J**) Recording paradigm for IPSCs evoked by direct application of GABA to mitral cells using a Picospritzer. (**K** to **M**) The *Cbln1* deletion severely impairs mitral cell IPSCs elicited by direct application of GABA [(K) representative traces; (L) summary plot of the total IPSC charge elicited by different application durations of GABA (10 μM); (M) summary graph of the slopes of the GABA response curve]. Data are means ± SEM (numbers of cells per mice analyzed are indicated above sample traces). Statistical significance was assessed by Student's *t* test (D to G and M) or by two-way ANOVA with Bonferroni test (C, I, and L), with $^*P < 0.05$, $^{**}P < 0.01$, $^{***}P < 0.001$, and $^{****}P < 0.0001$.

would enhance "silent" inhibitory synapses and make mIPSCs less detectable. Thus, we needed to determine whether the *Cbln1* deletion induced a synapse loss in the OB, as had been observed for the *Cbln1* deletion in the cerebellum (*36*, *44*).

The *Cbln1* deletion has no effect on synapse numbers or ultrastructure

Using cryosections from mice with a *Cbln1* deletion in mitral/tufted cells, we stained dendrodendritic synapses on mitral cells for vGAT as a universal inhibitory synapse marker and for synaptophysin-2 as a specific GC➔MC synapse marker (Fig. 4, A and B) (*45*). We observed no change in the number or size of inhibitory synapses in the external plexiform layer of mice with a *Cbln1* deletion in mitral/tufted cells, suggesting that the *Cbln1* deletion does not alter inhibitory synapse numbers (Fig. 4, A to F).

Some granule cells form synapses on the soma of mitral cells (*46*). These synapses are also stimulated in our GABA puffing experiment. Therefore, a specific loss of somatic inhibitory synapses could be caused by the *Cbln1* deletion. To test this possibility, we specifically analyzed perisomatic synapses of mitral cells. We retrogradely labeled the mitral cell soma with fluorescently tagged cholera toxin B that was injected into the piriform cortex and stained presynaptic granule cell inputs using synaptophysin-2 staining. Again, we observed no change in synapse numbers on *Cbln1*-deficient mitral cells (Fig. 4, G to I).

Last, to independently confirm the immunohistochemistry conclusions and to test whether the *Cbln1* deletion affects the structure of dendrodendritic synapses, we analyzed dendrodendritic synapses by electron microscopy (EM) (Fig. 4J). The *Cbln1* deletion in mitral cells produced no change in the density of dendrodendritic

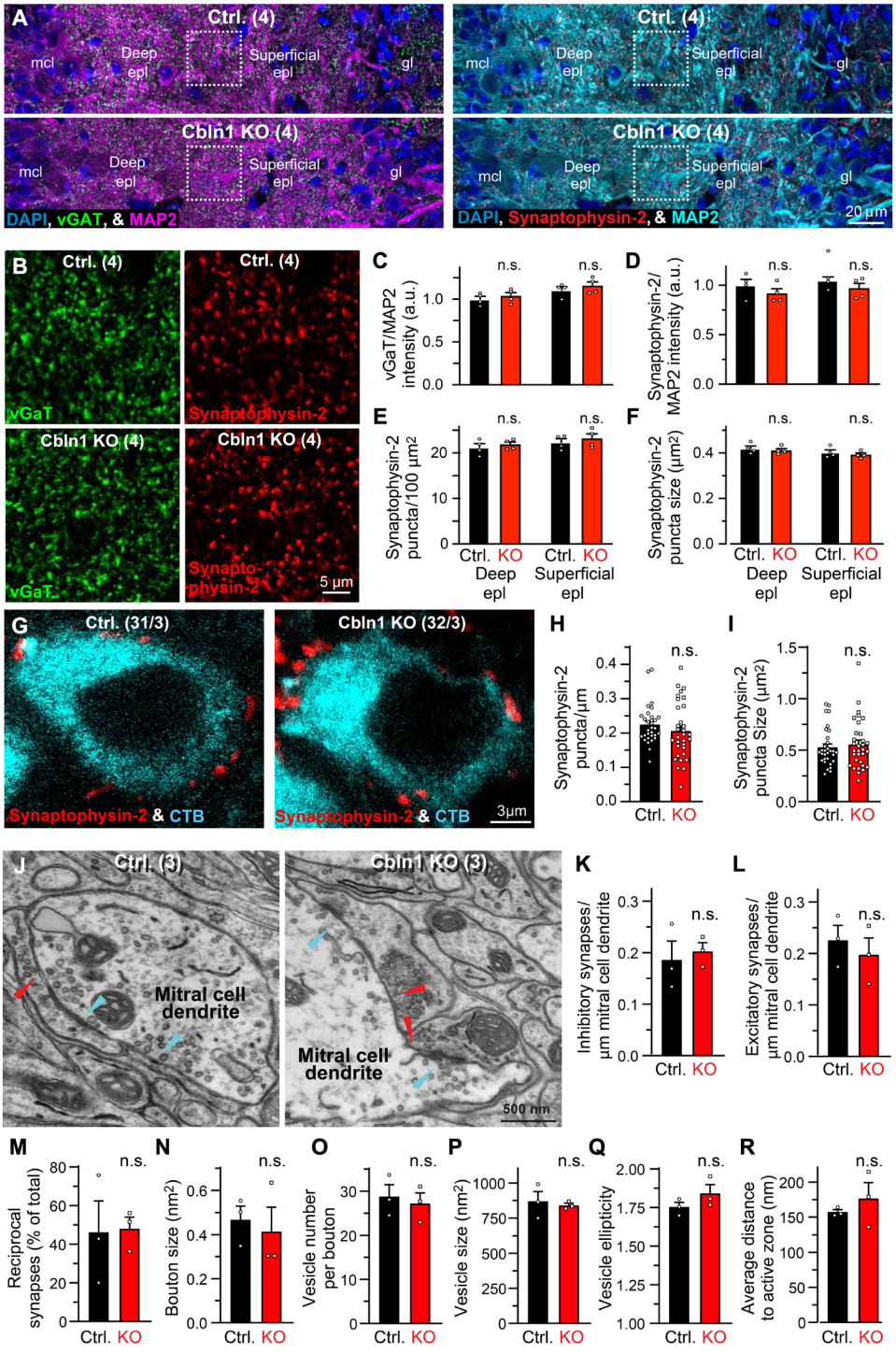

Fig. 4. *Cbln1* deletion from mitral and tufted cells does not significantly alter the density or ultrastructure of dendrodendritic synapses. (**A** to **F**) *Cbln1* deletion from mitral/tufted cells does not decrease vGAT- or synaptophysin-2–positive synapses on mitral cells [(A and B) representative low- and high-magnification images of OB sections stained for vGaT, synaptophysin-2, and MAP2 as indicated; (C) summary graph of the vGAT staining intensity; (D to F) summary graphs of the staining intensity, density, and size of synaptophysin-2–positive puncta. $N = 4$ mice. (**G** to **I**). *Cbln1* deletion does not lower the number of inhibitory perisomatic synapses onto mitral cells. Mitral cells were labeled by injecting fluorescent chloral toxin B (CTB) into the piriform cortex [(G) representative images; (H and I) the density and size of synaptophysin-2–positive puncta]. $N = 31$ and 32 cells from three mice. (**J** to **R**). EM shows that the *Cbln1* deletion does not alter the density or ultrastructure of dendrodendritic synapses {(J) representative images (red arrowheads, symmetric GC➔MC synapses; cyan arrowheads, asymmetric MC➔GC synapses); (K and L) inhibitory and excitatory synapse densities normalized for mitral cell dendrite length; (M) percentage of reciprocal synapses among inhibitory synapses; (N to R) ultrastructural parameters of reciprocal synapses [(N) bouton size; (O) vesicle numbers/bouton; (P) vesicle size; (Q) vesicle ellipticity; (R) vesicle-active zone distance of inhibitory synapses]}. $N = 3$ mice. Data are means ± SEM. Statistical analyses were performed by Student's *t* test in (H) to (R) and by two-way ANOVA with Bonferroni test in (C) to (F) (n.s., $P > 0.05$).

synapses on mitral cell dendrites, confirming the immunohistochemistry results (Fig. 4, K to M). Moreover, we detected no change in any structural parameter of synapses, such as the size of presynaptic terminals (Fig. 4N), the number of vesicles per terminal (Fig. 4O), the size of vesicles (Fig. 4P), the ellipticity of vesicles (Fig. 4Q), or the average distance of vesicles to the active zone (Fig. 4R). Thus, Cbln1 is essential in mitral cells as a postsynaptic regulator of GC➔MC synapses that controls the $GABA_A$ receptor responses of mitral cells without affecting either the release probability or the number of GC➔MC synapses.

Neuroligins are also essential for GC➔MC synaptic transmission

Because both neuroligins and Cbln1 are ligands for neurexins and because neuroligins are also abundantly expressed in mitral cells (Fig. 1H) (*47*), we next asked whether neuroligins contribute to the function of GC➔MC synapses in the OB. In mammals, neuroligins are encoded by four genes, *Nlgn1-4* (*48*–*51*). To test whether neuroligins function at GC➔MC synapses, we used *Nlgn1234* quadruple cKO (qcKO) mice. In these mice, the *Nlgn1*, *Nlgn2*, and *Nlgn3* genes are floxed and can be inactivated by Cre recombinase, whereas the *Ngln4* gene is constitutively deleted (*52*–*55*). We used these mice, instead of individual neuroligin KO mice, for the analysis of neuroligin function in mitral cells because multiple neuroligins often operate in the same synapse and are partly redundant (*52*) and because analysis of individual KO mice would be more time-consuming.

Using stereotactic injections, we introduced into the piriform cortex of *Nlgn1234* qcKO mice a retrogradely transported adeno-associated virus [rAAV2-retro; (*56*)] that coexpresses enhanced green fluorescent protein (EGFP) with Cre or ΔCre (mutant inactive Cre as a control) (Fig. 5A). rAAV2-retro infects axons in the piriform cortex that emanate from mitral/tufted cells in the OB, thereby enabling selective expression of Cre or ΔCre in mitral/tufted cells of the OB. Two to 3 weeks after injections, we analyzed the infected mitral cells in the OB electrophysiologically (Fig. 5B).

Recordings of mIPSCs from mitral cells showed that the deletion of all neuroligins produced a large reduction (~50%) in mIPSC frequency and a significant decrease (~20%) in mIPSC amplitude without changing the mIPSC kinetics (Fig. 5, C to G). As discussed above, most mIPSCs in mitral cells are derived from dendrodendritic GC➔MC synapses, suggesting that the neuroligin deletion impairs these synapses similar to the Cbln1 deletion. Analysis of evoked GC➔MC IPSCs revealed that the pan-neuroligin deletion caused a large reduction (~60%) in GC➔MC IPSC amplitudes and a significant increase in IPSC rise times but not decay times (Fig. 6, A to F). At the same time, the neuroligin deletions had no effect on the membrane capacitance or resistance of mitral cells, suggesting that it did not alter their size or viability (fig. S3).

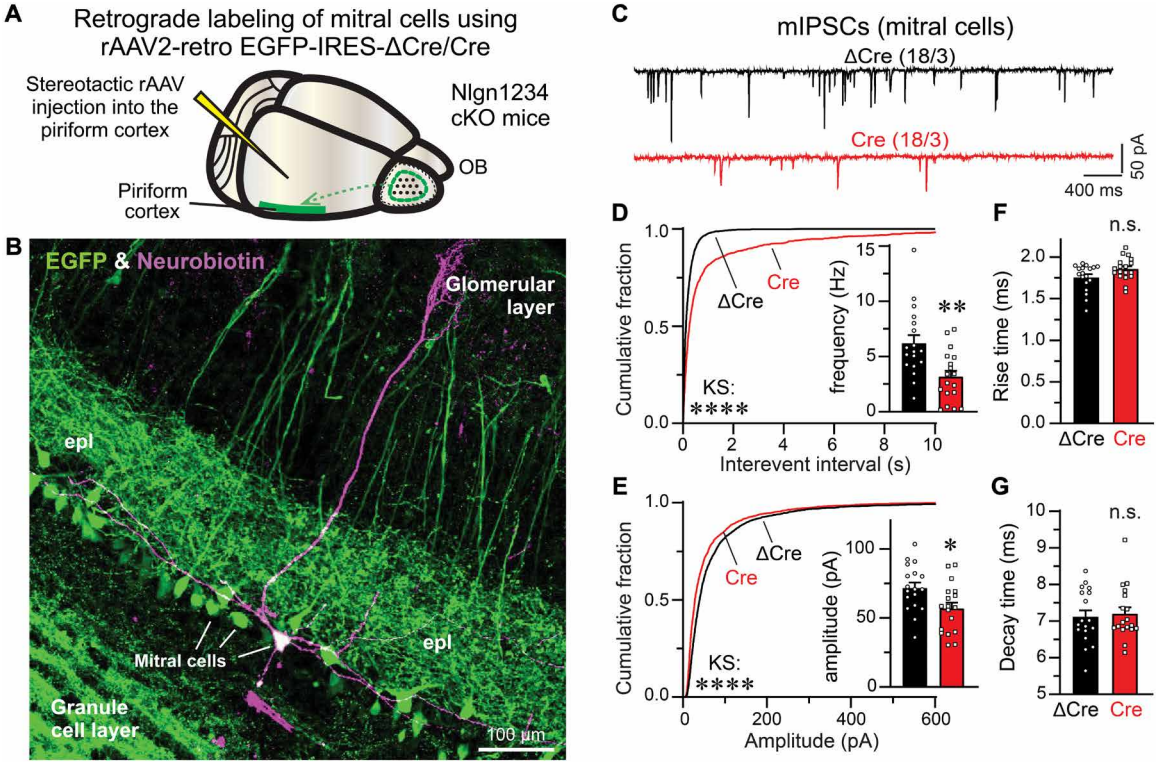

Fig. 5. Postsynaptic deletion of all neuroligins severely impairs synaptic inputs onto mitral cells. (**A**) Experimental strategy for selective infection of mitral cells of the OB by injecting rAAV2-retro coexpressing EGFP with ΔCre (control) or Cre into the piriform cortex. (**B**) Selective infection of mitral cells shown by EGFP with Neurobiotin filled during recording. (**C** to **G**) The *Nlgn1234* deletion decreases the mIPSC frequency and amplitude {(C) representative traces; (D and E) cumulative distribution of mIPSC interevent intervals (D) and amplitudes (E) [insets: mIPSC frequency (D) and amplitude (E) summary]; (F and G) mIPSC rise and decay times}. $N = 18$ cells from three mice (indicated in sample traces). Data are means ± SEM. Statistical analyses were performed by Kolmogorov-Smirnov tests in the cumulative distribution in (D) and (E) and by Student's *t* test in the bar graphs in (D) to (G) (*$P < 0.05$, **$P < 0.01$, and ****$P < 0.0001$).

We next asked whether the neuroligin deletion reduces GC➔MC synaptic transmission by a mechanism that is also similar to that of the *Cbln1* deletion. The pan-neuroligin deletion had no effect on the CV and PPR of eIPSCs (Fig. 6, G to I), suggesting that the release probability was unchanged. Similar to the *Cbln1* deletion, the neuroligin deletion robustly reduced (~50%) the amplitude of IPSCs evoked by direct application of GABA onto the mitral cell soma using a picospritzer (Fig. 6, J to M). Thus, the pan-neuroligin deletion suppresses postsynaptic $GABA_A$ receptor responses without affecting the presynaptic release probability, suggesting that neuroligins are essential organizers of GC➔MC synapses in the OB similar to Cbln1.

Alternative splicing of postsynaptic neurexins regulates GC➔MC synapses

Why are *Cbln1* and neuroligins both required for organizing GC➔MC synapses, although they bind to the same domain of neurexins? This requirement could operate by two mechanisms: a parallel involvement of postsynaptic *Cbln1* and neuroligins interacting with presynaptic granule cell neurexins in GC➔MC synapses, or a noncanonical function of Cbln1 or neuroligins acting on postsynaptic neurexins that indirectly renders GC➔MC synapses functional. This question is of general interest given that neurons often coexpress cerebellins and neuroligins but is particularly important for reciprocal synapses in which neurexins and neurexin ligands can potentially interact in both cis and trans configurations (Fig. 1B).

If mitral cell Cbln1 acted directly in GC➔MC synapses, then it would have to function by binding to presynaptic granule cell neurexins, whereas a noncanonical postsynaptic function would involve a binding to postsynaptic neurexins. Measurements of neurexin alternative splicing in mitral cell mRNAs using junction-flanking PCR showed that neurexins are predominantly expressed in mitral/tufted cells as splice site 4 containing (SS4+) variants (Fig. 7, A and B).

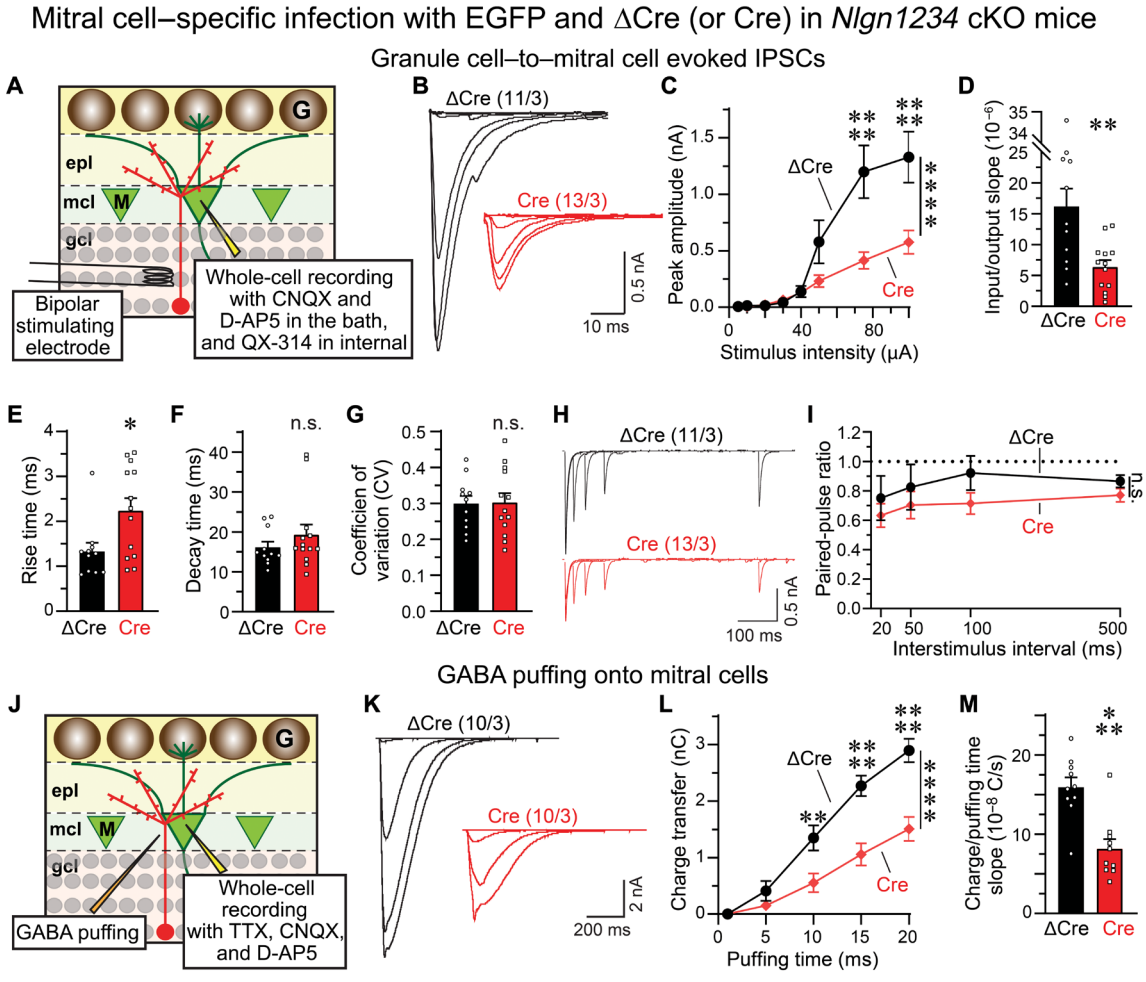

Fig. 6. Deletion of all neuroligins in mitral cells severely impairs GC➔MC synaptic transmission by suppressing the postsynaptic GABA receptor response similar to the *Cbln1* deletion. (**A**) Experimental paradigm for recordings of IPSCs evoked by stimulation of granule cell dendrites using an extracellular concentric bipolar electrode. (**B** to **D**) The *Nlgn1234* deletion impairs GC➔MC synaptic transmission [(B) representative traces; (C) input/output curve of GC➔MC IPSC peak amplitudes as a function of the stimulus intensity; (D) slope of the input/output curves]. (**E** and **F**) The *Nlgn1234* deletion slows down the kinetics of GC➔MC IPSCs [(E) rise time; (F) decay time]. (**G** to **I**) The *Nlgn1234* deletion has no effect on the CV (G) or the PPR [representative traces in (H) and summary graph in (I)] of GC➔MC IPSCs. (**J**) Experimental paradigm for recording GABA-mediated responses with direct application of GABA to mitral cells using a Picospritzer. (**K** to **M**) The *Nlgn1234* deletion decreases the magnitude of GABA-mediated response [(K) representative traces; (L) total charge elicited by different application durations of GABA; (M) slope of the GABA response curve). Data are means ± SEM (numbers of cells per mice indicated in sample traces). Statistical analyses were performed by Student's *t* test in (D) to (G) and (M) and by two-way ANOVA with Bonferroni test in (C), (I), and (L) (**P* < 0.05, ***P* < 0.01, ****P* < 0.001, and *****P* < 0.0001).

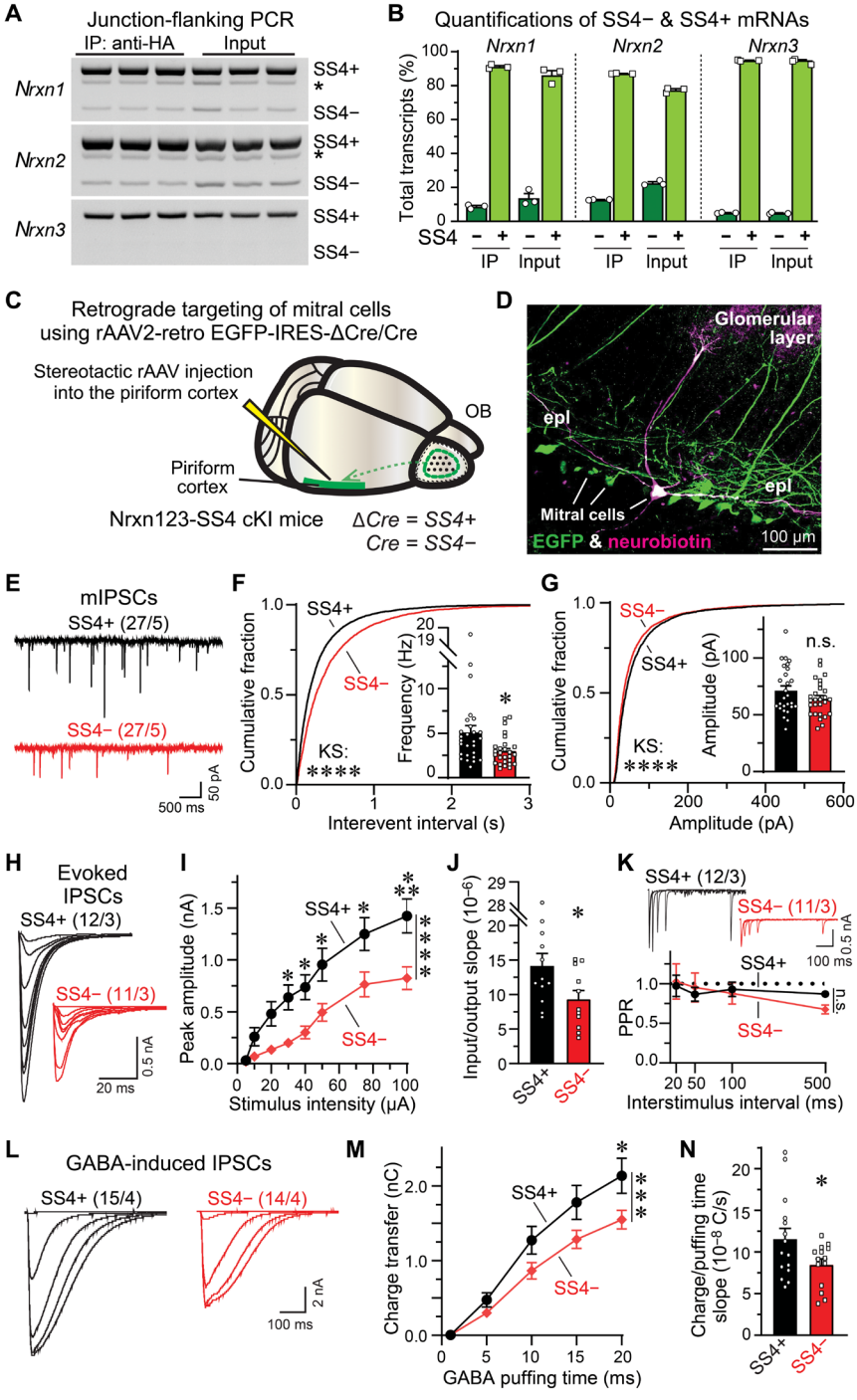

Fig. 7. Converting SS4+ neurexins in mitral cells into SS4– neurexins severely impairs GC→MC synaptic transmission similar to *Cbln1* and *Nlgn1234* deletions. (**A** and **B**) Nrxn1-3 are predominantly expressed as SS4+ variants in mitral/tufted cells [(A) representative image of junction-flanking PCR analyses of total OB mRNA (input) and RiboTag-isolated mitral/tufted cell mRNA [immunoprecipitation (IP): anti-HA] (see Fig. 1C; *, nonspecific band); (B) quantification of (A)]. (**C**) Experimental strategy. Mitral cell axons in the piriform cortex of triple SS4+ conditional knockin (cKI) mice were infected with retro-AAVs expressing ΔCre-EGFP (retaining SS4+ neurexins) or Cre-EGFP (converting SS4+ into SS4– neurexins). See (*59*). (**D**) Representative image of retrogradely infected mitral cells expressing EGFP, with a patched cell filled with Neurobiotin. (**E** to **G**) Conversion of SS4+ neurexins into SS4– neurexins decreases the mIPSC frequency {(E) representative traces; (Fand G) cumulative distribution of mIPSC interevent intervals (F) and amplitudes (G) [insets: summary graphs of the mIPSC frequency (F) and amplitude (G)]}. (**H** to **K**) Conversion of SS4+ neurexins into SS4– neurexins weakens evoked GC➔MC IPSCs without changing the PPR [(H) representative traces; (I and J) input/output curve and input/output slopes, respectively; (K) representative traces (top) and summary graph (bottom) of PPRs). (**L** to **N**) Conversion of SS4+ neurexins into SS4– neurexins decreases responses elicited by direct GABA application [(L) representative traces; (M and N) input/output curve and input/output slopes, respectively]. Data are means ± SEM [$n = 3$ mice in (A) and (B); numbers of cells per mice are indicated above the sample traces in (E) to (N)]. Statistical analyses were performed by Kolmogorov-Smirnov tests in (F) to (G); by Student's t test in (F), (G), (J), and (N); and by two-way ANOVA with Bonferroni test in (I), (K), and (M), with $^*P < 0.05$, $^{**}P < 0.01$, $^{***}P < 0.001$, and $^{****}P < 0.0001$.

This is important because only SS4+ variants of neurexins can bind Cbln1, whereas SS4− variants cannot (*36*, *57*, *58*).

Motivated by this finding, we tested whether converting the SS4+ variants of neurexins in mitral cells into SS4− variants that block their binding to Cbln1 but not to neuroligins suppresses GC➔MC synaptic transmission similar to the *Cbln1* deletion. For this purpose, we used triple-conditionally mutant mice that constitutively express all neurexins as SS4+ variants [*Nrxn123-SS4+* conditional knockin (cKI) mice] (*59*). In these mice, Cre recombinase converts the SS4+ neurexin variants into SS4− variants. We injected rAAV2-retro's coexpressing EGFP with ΔCre (control, retains SS4+ neurexin expression) or Cre (converts SS4+ neurons into SS4− neurexins) into the piriform cortex of *Nrxn123-SS4+* cKI mice and analyzed EGFP-positive mitral cells in acute slices by whole-cell patch-clamp recordings 2 to 3 weeks later (Fig. 7, C and D).

The conversion of postsynaptic SS4+ to SS4− neurexins in mitral cells robustly decreased the mIPSC frequency (~40%) without inducing major changes in mIPSC amplitude or mIPSC kinetics (Fig. 7, E to G, fig. S4, A and B). Moreover, the SS4 conversion produced a highly significant reduction (~35%) in the amplitude of evoked GC➔MC IPSCs and increased both the rise and decay times of eIPSCs (Fig. 7, H to J, and fig. S4, C and D). No change in the CV or PPR was observed (Fig. 7K and fig. S4E). Similar to the deletion of *Cbln1* or neuroligins in mitral cells, the conversion of SS4+ to SS4− neurexins in mitral cells also decreased the amplitude of IPSCs induced by direct application of GABA (Fig. 7, L to N; ~25% decrease). No change in the mitral cell membrane properties was observed in any of these experiments (fig. S4, F and G).

The phenotype of the conversion of SS4+ to SS4− neurexins in mitral cells indicates that, unexpectedly, Cbln1 binding to neurexins acts postsynaptically in dendrodendritic GC➔MC synapses. However, the results do not completely rule out the possibility that Cbln1 also acts by binding to presynaptic neurexins in GC➔MC synapse, i.e., that the Cbln1/neurexin and neuroligin/neurexin signaling pathways operate in the same synapse simultaneously. To test this possibility, we converted SS4+ neurexins in granule cells into SS4− neurexins. We expressed Cre or ΔCre (as a control) in the OB of *Nrxn123*-SS4+ cKI mice using AAV_{DJ}'s under conditions that only infect granule cells (fig. S4, H and I). Rendering most granule cell neurexins SS4− had no effect on evoked GC➔MC IPSCs, indicating that presynaptic neurexins in GC➔MC synapses do not functionally require Cbln1 binding (fig. S4, J to S). Moreover, CRISPR-mediated deletion of postsynaptic GluD1 in mitral cells had no effect on GC➔MC synapses (fig. S5). Here, the lack of an effect might have been due to redundancy between GluD1 and GluD2 because of GluD2 enrichment in mitral/tufted cells (Fig. 1F). However, it was shown that GluD1 rather than GluD2 preferentially induces inhibitory presynaptic differentiation (*60*) and that GluD2 deletion increases rather than decreases inhibitory synapse number in the cerebellum (*38*). Viewed together, these observations argue against the possibility that Cbln1 mediates GC➔MC synapses through a trans-synaptic complex involving presynaptic granule cell neurexins and postsynaptic mitral cell GluD1.

Cbln1 prevents inhibition of neurexin/neuroligin trans interactions by neurexin/ neuroligin cis interactions

Viewed together, our data suggest that Cbln1 and neuroligin function postsynaptically in GC➔MC synapses and that this function requires postsynaptic SS4+ variants of neurexins and is abolished by SS4− variants of neurexins. A plausible model to explain these data is that Cbln1 is essential in dendrodendritic GC➔MC synapses because it blocks a cis neurexin/neuroligin interaction that would otherwise inhibit postsynaptic neuroligins in this synapse. Cis interactions of neurexins with neuroligins and cerebellins are structurally plausible because the neurexin LNS domain that binds to these ligands is separated from the membrane by a fairly large flexible linker. This model implies that Cbln1 competitively blocks neuroligins from binding to neurexins. To test this implication, we compared binding of Cbln1 tagged with an hemagglutinin (HA) epitope (HA-Cbln1) or of the extracellular domains of Nlgn1 fused to the immunoglobulin G Fc domain [Nlgn1-ECD (extracellular domain)–Fc] to the two SS4 splice variants of Nrxn1β ($Nrxn1\beta^{SS4+}$ and $Nrxn1\beta^{SS4-}$) (Fig. 8A). As expected, HA-Cbln1 only bound to $Nrxn1\beta^{SS4+}$ but not to $Nrxn1\beta^{SS4-}$, whereas Nlgn1-ECD-Fc bound to both (Fig. 8B). When HA-Cbln1 and Nlgn1-ECD-Fc were added sequentially, HA-Cbln1 blocked binding of Nlgn1-ECD-Fc to $Nrxn1\beta^{SS4+}$, independent of whether Cbln1 was bound to $Nrxn1\beta^{SS4+}$ first, or added after Nlgn1-ECD-Fc had been prebound (Fig. 8B). HA-Cbln1, however, had no effect on Nlgn1-ECD-Fc binding to $Nrxn1\beta^{SS4-}$ that is unable to bind cerebellins (Fig. 8B). Consistent with previous binding affinity measurement (*57*, *61*, *62*), these results show that Cbln1 binds more tightly to $Nrxn1\beta^{SS4+}$ than Nlgn1.

The binding data suggest that Cbln1 could prevent a cis interaction of neurexins with neuroligins and thereby function in reciprocal synapses by relieving the inhibition of mitral cell neuroligins that is induced by cis binding of neurexins (Fig. 1B). A competition between cerebellins and neuroligins for neurexin binding is likely because these two neurexin ligands bind to adjacent sequences close to the SS4 region of neurexins (*57*, *61*, *62*). To test this hypothesis, we examined the inhibitory effect of cis neurexin/neuroligin interactions on trans neurexin/neuroligin interactions and tested the possible role of Cbln1 in blocking this inhibition (Fig. 8C). We reconstituted cis versus trans neurexin/neuroligin interactions using cell aggregation assays with FreeStyle human embryonic kidney (HEK) 293 cells that coexpress Nrxn1β or Nlgn2 to mimic the expression observed in mitral cells (Fig. 1, E and H). We then tested the effect of the cis expression of $Nrxn1\beta^{SS4+}$ or $Nrxn1\beta^{SS4-}$ with Nlgn2 on the trans Nrxn1β/Ngln2 interaction in the absence and presence of Cbln1 (Fig. 8C). Although Nlgn2-expressing cells formed large cell aggregates with Nrxn1β-expressing cells, these aggregates were suppressed when Nrxn1β, independent of SS4, was also coexpressed in cis with Nlgn2. Hence, the cis Nrxn1β-Nlgn2 interaction impaired the trans Nrxn1β/Nlgn2 interaction without completely abolishing it (Fig. 8D). As a control, we coexpressed in cis Nrxn1β mutants that are unable to bind to neuroligins ($Nrxn1\beta^{SS4-*}$ or $Nrxn1\beta^{SS4+*}$). These mutants contain G155V and T156A substitutions that block neuroligin binding (*63*). Cis expression of Nrxn1β mutants, in contrast to wild-type Nrxn1β, had no effect on the trans Nrxn1β/Nlgn2 interaction (Fig. 8D).

When we coexpressed Nlgn2 not only with $Nrxn1\beta^{SS4+}$ or $Nrxn1\beta^{SS4-}$ but also with Cbln1, the coexpressed Cbln1 reversed the inhibition of the trans Nrxn1β/Nlgn2 interaction that was produced by cis expression of $Nrxn1\beta^{SS4+}$ but not the inhibition that was produced by cis expression of $Nrxn1\beta^{SS4-}$ (Fig. 8D). These data demonstrate that a cis neurexin/neuroligin interaction inhibits trans neurexin/neuroligin interactions and that this inhibition is alleviated when a cerebellin is coexpressed in cis with the neurexin and neuroligin, as long as the isoform of neurexin used is capable of

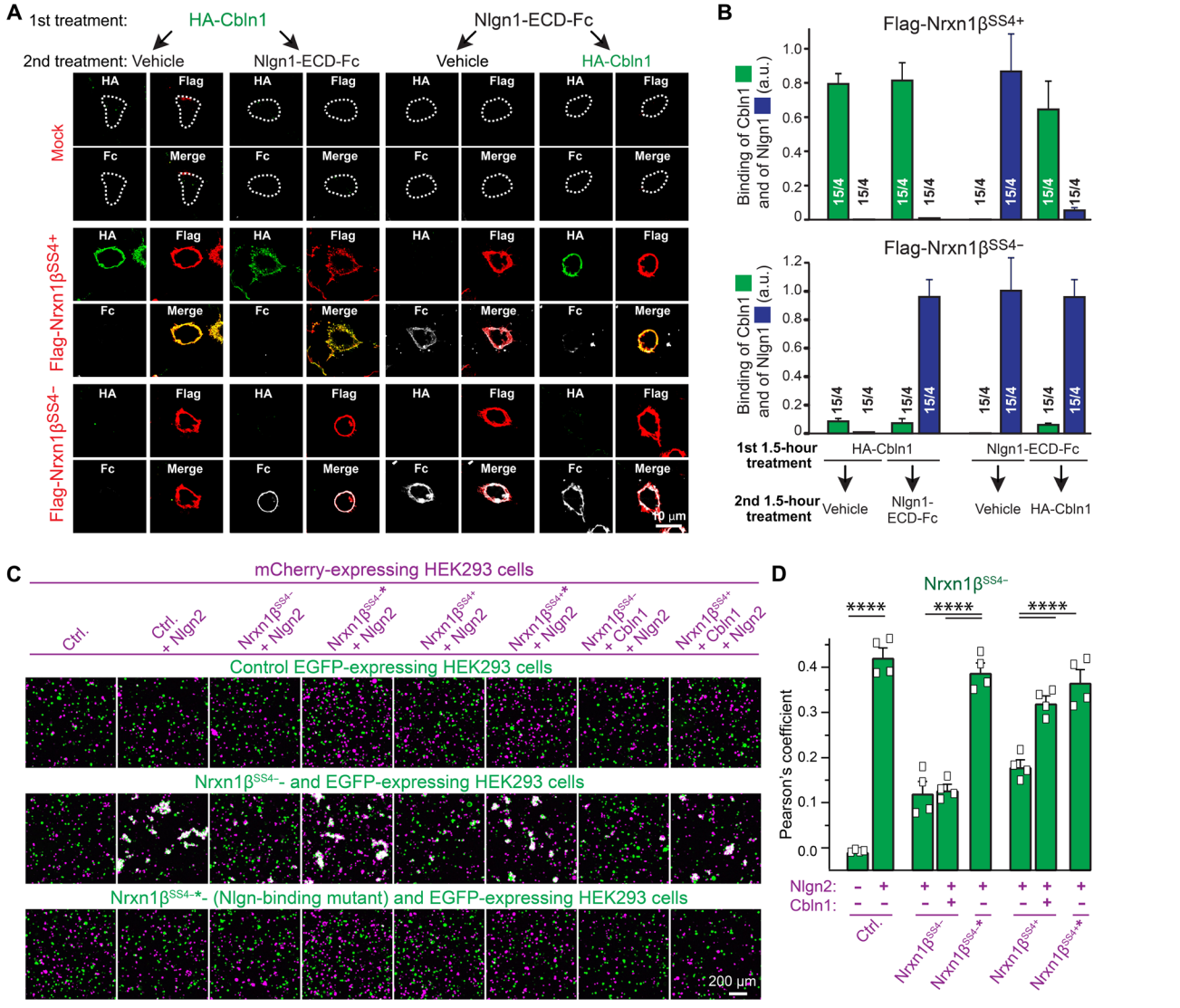

Fig. 8. Cbln1 displaces Nlgn1 from the SS4+ but not the SS4– splice variant of Nrxn1β and largely reverses the cis Nrxn1β–mediated inhibition of trans Nrxn1β/Nlgn2 interactions. (**A**) Representative images of HEK293 cells transfected with Flag-tagged Nrxn1β^{SS4+}, Nrxn1β$^{SS4–}$, or a mock control and sequentially incubated for 1.5 hours first with HA-Cbln1 or Nlgn1-ECD-Fc and second with vehicle, Nlgn1-ECD-Fc, or HA-Cbln1 as indicated. Binding of HA-Cbln1 and Nlgn1-ECD-Fc to the surface-exposed Nrxn1β was visualized by immunocytochemistry in nonpermeabilized cells. (**B**) Demonstration that Cbln1 prevents and competes off binding of Nlgn1-ECD-Fc to Nrxn1β^{SS4+} but not to Nrxn1β$^{SS4–}$ [summary graphs of surface binding of HA-Cbln1 (green) or Nlgn1-ECD-Fc (blue) to Nrxn1β^{SS4+} or Nrxn1β$^{SS4–}$]. The *y* axis depicts the ratio of fluorescence signal intensity of neurexin ligands over neurexin signals on HEK cell surface. a.u., arbitrary units. (**C**) Representative images of FreeStyle HEK cells transfected with EGFP and mCherry together with respective synaptic organizer molecules. Nrxn1β* denotes Nrxn1β with Nlgn binding mutations (G155V and T156A). (**D**) Summary of Pearson's coefficients across different conditions. All numerical data are means ± SEM. Sample size is indicated by numbers of cells per culture batches in (B) in which fluorescence intensity from cells in each batch was averaged as one data point; $n = 4$ batches of culture were used in (C) and (D). Statistical analyses were performed by two-way ANOVA with Bonferroni's multiple comparison test in (D) (****$P < 0.0001$).

actually binding to the cerebellin. Hence, the two antiparallel neurexin signaling processes can interfere with each other, and Cbln1 can mediate their functional compartmentalization, underlying the mechanism for self-avoidance within the neurexin-interaction network.

Cbln1 in mitral cells mediates molecular self-avoidance in synaptic neurexin complexes at the reciprocal dendrodendritic synapses

Our data thus suggest a molecular logic for neurexin signaling despite its binding promiscuity, whereby Cbln1 blocks cis interactions of neurexins with neuroligins and thereby enables antiparallel trans interactions of neurexins and neuroligins. Via this mechanism, Cbln1 functionally separates pre- and postsynaptic signaling compartments. An inherent prediction of this hypothesis is that postsynaptic neurexins in mitral cells are not essential for GC➔MC synaptic transmission but rather function as presynaptic neurexins for the mitral cell➔granule cell synapses. This hypothesis also implies that the conversion of postsynaptic SS4+ neurexins into SS4– neurexins impairs GC➔MC synaptic transmission only because it prevents Cbln1 from blocking the cis interactions of postsynaptic

neurexins with neuroligins. To test this hypothesis directly, we deleted all neurexins (except for Nrxn1γ that does not bind to either Cbln1 or neuroligins) (*27*) from mitral cells by injection of rAAV2-retro that coexpress EGFP with Cre or ΔCre (as a control) into the piriform cortex of *Nrxn123* triple cKO mice (*64*) and analyzed GC➔MC synapses in acute slices by mitral cell recordings (Fig. 9A). As predicted by the hypothesis, the postsynaptic deletion of neurexins had no effect on synaptic transmission, and thus, postsynaptic neurexins are functionally compartmentalized from the adjacent antiparallel neurexin-neuroligin signaling process (Fig. 9, B to D, and fig. S7).

In a final test of this hypothesis, we overexpressed in mitral cells either wild-type Nrxn1β^{SS4-} and Nrxn1β^{SS4+} or mutant Nrxn1β^{SS4-}* and Nrxn1β^{SS4+}* that are unable to bind to neuroligins (Figs. 8, C and D, and 10A) (*63*). We again injected rAAV2-retro into the piriform cortex to selectively express the various neurexins in mitral cells of the OB (Fig. 10, B and C). Overexpression of Nrxn1β^{SS4-} and Nrxn1β^{SS4+} inhibited GC➔MC synaptic transmission as measured by eIPSCs, whereas overexpression of mutant Nrxn1β^{SS4-}* and Nrxn1β^{SS4+}* had no effect (Fig. 10, D to F, and fig. S8, A to G). In these experiments, even Nrxn1β^{SS4+} was inhibitory despite its binding to Cbln1 probably because the Nrxn1β^{SS4+} overexpression levels exceeded those of endogenous Cbln1. Hence, we tested the effect of co-overexpression of Cbln1 and Nrxn1β^{SS4-} (or Nrxn1β^{SS4+}). Expectedly, Cbln1 overexpression in mitral cells likely saturates binding of Nrxn1β^{SS4+} and hence occludes its dominant negative effect, but not for Nrxn1β^{SS4-} (Fig. 10, G to I, and fig. S8, H to N). To test the physiological relevance of Cbln1 in the cis inhibition by Nrxn1β, we overexpressed Nrxn1β^{SS4-} and Nrxn1β^{SS4+} on the background of the *Cbln1* deletion. Because Nrxn1β overexpression in mitral cells exerts its dominant negative effect through interacting with neuroligins in cis (Fig. 10, D to F), the lack of additive effects when overexpressing Nrxn1β on the *Cbln1* deletion background argues that the *Cbln1* deletion permits the formation of endogenous cis neurexin-neuroligin complexes (Fig. 10, J to L, and fig. S8, O to U). Thus, Cbln1 functionally compartmentalizes two antiparallel neurexin signaling processes by preventing cis neurexin/neuroligin interactions at the reciprocal dendrodendritic synapses in the OB.

DISCUSSION

Neurexins are presynaptic organizer molecules that, via diverse and highly regulated interactions with an expansive panoply of postsynaptic ligands, regulate multiple pre- and postsynaptic functional properties (*6*). As arguably the best characterized synaptic organizer molecule, neurexins serve as a paradigm for how trans-synaptic adhesion complexes shape synapse assembly. Thus, we used neurexins in the present study to examine how trans-synaptic adhesion complexes organize nonstandard synapses in which pre- and postsynaptic specializations are formed in close proximity on the same plasma membrane domain, such as is observed in reciprocal synapses and axo-axonic synapses on presynaptic terminals. Our results delineate a simple mechanism of self-avoidance that blocks the formation of cis complexes for neurexins that are simultaneously presynaptic and postsynaptic in reciprocal and axo-axonal synapses and enables the formation of trans complexes in these synapses. This mechanism consists of prevention of neurexin-neuroligin cis complexes by the binding of postsynaptic Cbln1 to the neurexins, with the resulting antiparallel neurexins engaging in trans complexes with neuroligins to enable functional synapse assembly.

Nonstandard synapses, such as reciprocal and axo-axonic synapses in which pre- and postsynaptic specializations are colocalized to the same plasma membrane domain, are an essential part of neural circuits throughout the brain, usually as an inhibitory pathway. Reciprocal dendrodendritic synapses are particularly important in the OB for olfactory information processing, where they process the incoming olfactory information that is transferred by mitral cells from the glomeruli to various central olfactory regions (*14*, *15*). Here, we studied the function of neurexins and their ligands in these reciprocal synapses as a model system to gain insight into how trans-synaptic complexes are assembled when cis-synaptic complexes would be favored. We show that, in mitral cells, Cbln1 is essential for GC➔MC synaptic transmission because Cbln1 blocks the cis interaction of postsynaptic mitral cell neurexins with neuroligins. When *Cbln1* is deleted and this cis interaction is enabled, the trans-synaptic binding of postsynaptic mitral cell neuroligins with presynaptic granule cell neurexins is abolished, and GC➔MC synaptic transmission is impaired.

The evidence for this conclusion is as follows. First, we show that, in mitral cells, Cbln1 is essential for the organization of GC➔MC synapses. Cbln1 is not required for the establishment or maintenance of GC➔MC synapses or for regulating the presynaptic release probability but instead enables a physiological postsynaptic $GABA_A$ receptor response (Figs. 2 to 4). Second, we demonstrate that neuroligins are also essential for a normal postsynaptic $GABA_A$ receptor response without a role in the presynaptic release probability (Figs. 5 and 6). Third, we showed that mitral cells express almost only SS4+ variants of neurexins that bind to Cbln1 and that

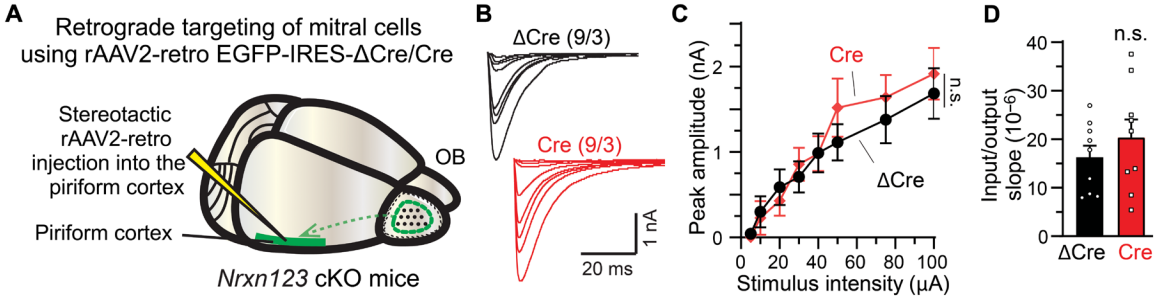

Fig. 9. Postsynaptic neurexins in mitral cells are not essential for GC➔MC synaptic transmission. (**A**) Experimental strategy for the postsynaptic deletion of all neurexins in mitral cells of *Nrxn123* triple cKO mice. (**B** to **D**) Postsynaptic deletion of neurexins does not impair GC➔MC synaptic transmission [(B) representative traces of GC➔MC eIPSCs; (D and E) input/output curve and slope summary]. $N = 9$ cells from three mice as indicated in sample traces. Data are means ± SEM. Statistical analyses were performed by Student's *t* test in (D) and by two-way ANOVA with Bonferroni test in (C) (n.s., $P > 0.05$).

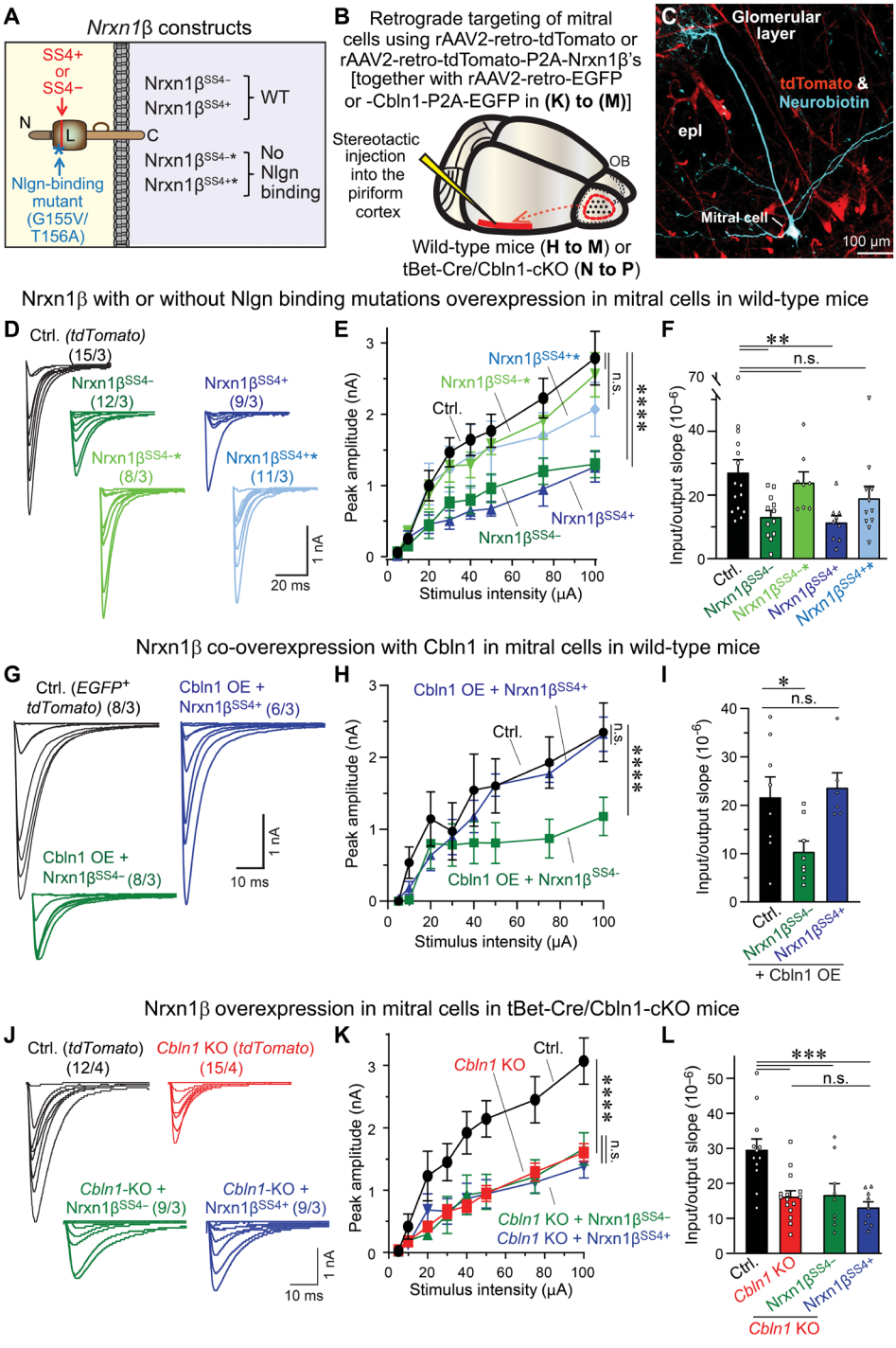

Fig. 10. Genetic epistasis with Nrxn1β overexpression in mitral cells reveals that Cbln1 prevents the formation of endogenous *cis* neurexin-neuroligin complexes. (**A**) Schematic of the Nrxn1β domain structure and overview of the Nrxn1b constructs used for overexpression experiments in mitral cells in (**D**) to (**L**). (**B**) Experimental strategy for the postsynaptic overexpression of Nrxn1β constructs in mitral cells. Nrxn1β was fused to tdTomato using P2A to label infected cells. (**C**) Selective infection of mitral cells shown by tdTomato with Neurobiotin filled during recording. (D to F). Postsynaptic Nrxn1β overexpression in mitral cells inhibits GC➔MC synaptic transmission for the wild-type Nrxn1β $^{SS4+}$ and Nrxn1β $^{SS4-}$ but not for mutant Nrxn1β^{SS4+}* and Nrxn1β^{SS4-}* that are unable to bind to neuroligins. [(D) representative traces of GC➔MC eIPSCs; (E and F) input/output curve and slope summary]. Note that Nrxn1β^{SS4+} likely inhibits despite the presence of Cbln1 because Cbln1 levels are insufficient to saturate binding of Nrxn1β^{SS4+}. (G to I) The inhibition of GC➔MC synaptic transmission by overexpressed Nrxn1β^{SS4+} but not Nrxn1β^{SS4-} is occluded by Cbln1 overexpression (OE) [similar arrangement to (D) to (F)]. Cbln1 overexpression is achieved through rAAV2-retro expressing Cbln1-P2A-EGFP injected in the piriform cortex. (J to L) The inhibition of GC➔MC synaptic transmission by overexpressed Nrxn1β^{SS4+} and Nrxn1β^{SS4-} is occluded by prior deletion of *Cbln1* [similar arrangement to (D) to (F)]. Data are means ± SEM (numbers of cells per mice analyzed are indicated above the sample traces). Statistical analyses were performed by one-way ANOVA in (F), (I), and (L) and by two-way ANOVA in (E), (H), and (K). Multiple comparison tests are done with Bonferroni approaches (*$P < 0.05$, **$P < 0.01$, ***$P < 0.001$, and ****$P < 0.0001$).

converting mitral cell SS4+ neurexins into SS4− neurexins impairs GC➔MC synapses in the same manner as the Cbln1 and the neuroligin deletions (Fig. 7). Fourth, we describe that Cbln1 displaces Nlgn1 from Nrxn1β on the cell surface as long as Nrxn1β is expressed as an SS4+ variant that binds Cbln1, that Nrxn1β—when expressed in *cis* with Nlgn2—suppresses the trans interaction of Nlgn2 with Nrxn1β present on another cell, and that this suppression is alleviated by coexpression of Cbln1 (Fig. 8). Last, we documented that postsynaptic neurexins in mitral cells are not essential for GC➔MC synaptic transmission but that overexpression of postsynaptic Nrxn1β impairs GC➔MC synapses as long as the overexpressed Nrxn1β is able to bind to neuroligins and that the impairment from overexpression depends on Cbln1 in a neurexin SS4-dependent manner (Figs. 9 and 10).

Our study thus describes a mechanism that enables assembly of separate trans-synaptic neurexin complexes between vicinal reciprocal synapses. Our data thereby establish that the context-dependent function of neurexins depends not only on the transcriptomic signatures of the involved neuron and glia populations at a given circuit but also on the relative binding affinities of the synaptic organizers involved as well as their posttranscriptional and posttranslational modifications that alter their biochemical properties.

Our work highlights the importance of multiple trans-synaptic signaling pathways at a given synapse. Most molecular and genetic studies on synaptic organizer molecules focus on components of one given trans-synaptic complex at a time (*1*, *6*, *23*). However, multiple molecular machineries likely operate in parallel, with or without lateral interactions, at all synapses to mediate synapse formation and to regulate their properties. Trans-synaptic molecular networks are likely organized similar to logic gates, with divergent and convergent signaling pathways and AND/OR/NOT decision points. Dissecting these functional networks is a painstakingly slow process that requires nonscalable, technically demanding methods, such as high-resolution electrophysiology or imaging. The molecular design principle for the reciprocal synapses shown here provides a first step toward such a dissection and represents the first analysis of the relation of multiple synaptic adhesion interactions but much more remains to be done.

MATERIALS AND METHODS

Mouse husbandry

For confirming the specificity of the *tBet-Cre* line, hemizygous *tBet-Cre* mice were crossed with *Ai14* mice (*30*, *31*). For analyzing mitral/tufted cell–specific translating mRNA, RiboTag mice were crossed with hemizygous *tBet-Cre* mice (*30*, *32*). For mitral/tufted cell–specific *Cbln1* deletion, *Cbln1* homozygous cKO mice were crossed with *Cbln1* homozygous cKO mice with one *tBet-Cre* allele (*30*, *34*). *Nlgn1234* qcKO mice (*52*), *Nrxn123* SS4 cKI mice (*59*), *Nrxn123* cKO mice (*64*), and Cas9 KI mice (*65*) were generated as described in respective previous studies. Mice were group-housed (maximum of five mice per cage) and maintained on a 12-hour light–dark cycle (7 a.m. to 7 p.m., light), with access to food and water ad libitum. Age- and gender-matched littermates were used for experiments, except for the Nrxn1β overexpression experiments in Fig. 8, where the number of mice required made it impossible and only age-matched littermates were used. All experiments involving animals were approved by the Stanford Animal Use Committees [Administrative Panel for Laboratory Animal Care (APLAC/) Institutional Animal Care and Use Committee (IACUC)].

Purification of OB mRNA

Mice were euthanized using isoflurane and decapacitated. The OBs were quickly dissected and snap-frozen in liquid nitrogen or dry ice and transferred to −80°C storage until processing. The specimen was subjected to RNA extraction using the QIAGEN RNeasy Micro kit.

Purification of mitral/tufted cell–specific mRNA

RiboTag mice were crossed with *tBet-Cre* mice (*30*, *32*). After OB extraction described above, the frozen bulbs were partially thawed in fresh homogenization buffer at 10% (w/v) and Dounce homogenized. Homogenates underwent centrifugation, and 10% of the supernatant was used as input. The remaining supernatant was incubated with prewashed anti-HA magnetic beads (Thermo Fisher Scientific) overnight at 4°C. The beads were washed three times with a high-salt buffer followed by elution with RLT lysis buffer containing 2-mercaptoethanol. The sample and the input were then subjected to mRNA extraction described above.

Quantitative real-time PCR

Quantitative reverse transcription (RT)–PCR was performed in triplicates for each condition with QuantStudio 3 (Thermo Fisher Scientific). RNA (20 ng) was used each reaction, in conjunction with TaqMan Fast Virus 1-Step Master Mix (Thermo Fisher Scientific) and gene-specific qRT-PCR probes [IDT (integrated DNA technologies)] as described previously (*66*). Predesigned PrimeTime qPCR probe assays (IDT) were used for vGluT1 (Mm.PT.58.12116555), vGaT (Mm.PT.58.6658400), aquaporin-4 (Mm.PT.58.9080805), MBP (Mm.PT.58.28532164), ActB (Mm.PT.39a.22214843.g), Cbln1 (Mm.PT.58.12172339), Cbln2 (Mm.PT.58.5608729), Cbln4 (Mm.PT.58.17207498), Grid1 (Mm.PT.58.32947175), and Grid2 (Mm.PT.58.12083939). Customed PrimTime qPCR probe assays (IDT) were used for Nrxn1α (forward: TTCAAGTCCACAGATGCCAG; reverse: CAACACAAATCACTGCGGG; probe: TGCCAAAACTGGTCCATGCCAAAG), Nrxn1β (forward: CCTGTCTGCTCGTGTACTG; reverse: TTGCAATCTACAGGTCACCAG; probe: AGATATATGTTGTCCCAGCGTGTCCG), Nrxn1γ (forward: GCCAGACAGACATGGATATGAG; reverse: GTCAATGTCCTCATCGTCACT; probe: ACAGATGACATCCTTGTGGCCTCG), Nrxn2α (forward: GTCAGCAACAACTTCATGGG; reverse: AGCCACATCCTCACAACG; probe: CTTCATCTTCGGGTCCCCTTCCT), Nrxn2β (forward: CCACCACTTCCACAGCAAG; reverse: CTGGTGTGTGCTGAAGCCTA; probe: GGACCACATACAT CTTCGGG), Nrxn3α (forward: GGGAGAACCTGCGAAAGAG; reverse: ATGAAGCGGAAGGACACATC; probe: CTGCCGTCATAGCTCAGGATAGATGC), Nrxn3β (forward: CACCACTCTGTGCCTATTTC; reverse: GGCCAGGTATAGAGGATGA; probe: TCTATCGCTCCCCTGTTTCC), Nlgn1 (forward: GGTTGGGTTTGGTATGGATGA; reverse: GATGTTGAGTGCAGTAGTAATGAC; probe: TGAGGAACTGGTTGATTTGGGTCACC), Nlgn2 (forward: CCGTGTAGAAACAGCATGACC; reverse: TGCCTGTACCTCAACCTCTA; probe: TCAATCCGCCAGACACAGATATCCG), and Nlgn3 (forward: CACTGTCTCGGATGTCTTCA; reverse: CCTCTATCTGAATGTGTATGTGC; probe: CCTGTTTCTTAGCGCCGGATCCAT).

Electrophysiology

Cbln1 cKO mice with or without *tBet-Cre* alleles were patched between postnatal day 21 (P21) and P28. For viral manipulations, mice were injected at P16 to P21. Two to 3 weeks after viral injection,

mice were anesthetized via isoflurane inhalation, and brains were quickly removed. The brain was sliced in ice-cold oxygenated (95% O_2 and 5% CO_2) cutting solution (228 mM sucrose, 11 mM glucose, 26 mM $NaHCO_3$, 1 mM NaH_2PO_4, 2.5 mM KCl, 7 mM $MgSO_4$, and 0.5 mM $CaCl_2$). Horizontal sections (300 μm thickness) were obtained using a vibratome and placed in oxygenated artificial cerebrospinal fluid (ACSF; 119 mM NaCl, 2.5 mM KCl, 1 mM NaH_2PO_4, 1.3 mM $MgSO_4$, 26 mM $NaHCO_3$, 10 mM glucose, and 2.5 mM $CaCl_2$) at 32°C for 30 min. Slices were allowed to recover at room temperature for an additional 30 min. The recording chamber was temperature controlled and set to 32°C, and ACSF was perfused at 1 ml/min. The internal solution for whole-cell patch clamp contained 135 mM CsCl, 10 mM Hepes, 1 mM EGTA, 1 mM Na–guanosine 5′-triphosphate, and 4 mM Mg–adenosine 5′-triphosphate pHed to 7.4. QX314-bromide (10 mM) was added for evoked recordings. Neurobiotin (0.2%; Vector Laboratories) was included for morphological reconstruction. The pipette resistance ranged from 1.8 to 2.5 megohm. Mitral cells were identified in the mitral cell layer, and access resistance was under 10 megohm throughout the experiment. Tetrodotoxin (TTX, 1 μM; Tocris) and picrotoxin (100 μM; Tocris) were included in the bath solution for mEPSC. TTX (1 μM; Tocris), 6-cyano-7-nitroquinoxaline-2,3-dione (CNQX, 20 μM; Tocris), and D-AP5 (50 μM; Tocris) were included in the bath for mIPSC and GABA puffing. CNQX (20 μM; Tocris) and D-AP5 (50 μM; Tocris) were included in the bath for eIPSC recordings. GC➔MC eIPSCs were recorded at −70 mV with a concentric bipolar electrode placed directly below the mitral cell with constant distance roughly at the junction between internal plexiform layer and granule cell layer, 30 μm below the surface of the slice. PGC➔MC eIPSCs were recorded by placing the concentric bipolar electrode on the glomerulus containing the dendrites of the recorded mitral cell, which were visualized by including Alexa Fluor 488 in the internal solution. The same concentric bipolar electrodes were used for each experiment. However, different concentric bipolar electrodes were used across different experiments as they wear out, and this variability might cause the differences in absolute value of eIPSC observed. The kinetics, CV, and PPR of GC➔MC eIPSC were all monitored at 75-μA stimulus intensity. For GABA puffing, 10 μM GABA (Tocris) dissolved in the bath solution were loaded in glass pipette with resistance of 1.8 to 2.5 megohm and connected to the Picropritzer. The GABA-containing pipette was placed on the same level of the mitral cell soma with constant distance (~10 μm). GABA puff was delivered with 10 psi of various durations. All recordings were analyzed in Clampfit after applying a 500-Hz Gaussian filter. Rise time was defined as the time from 10 to 90% of peak amplitude, and decay time was defined as the time from 90 to 10% of peak amplitude. The experimenter was blind to the treatment groups during recordings and analysis.

AAV preparation

The AAV serotype used in this study was AAV-DJ, as well as rAAV2-retro for retrograde tracing experiments (*55*). HEK293T cells were transfected with the AAV vector, the helper plasmid, and the serotype-specific capsid plasmids by using calcium phosphate. Cells were harvested 72 hours after transfection. Nuclei were lysed, were treated with Benzonase nuclease (Sigma-Aldrich, catalog no. E1014), and underwent iodixanol gradient ultracentrifugation (3 hours at 65,000 rpm using a S80AT3 rotor). AAV were then concentrated and dialyzed in minimal essential medium. For CRISPR-Cas9–mediated deletion of GluD1, a pair of control guides (AAACACCGGAAGAGCGAGCTCTTCTGTT; CACCAGAGACCGAGGTCTCGGTT) or Grid1-targeting guides (GCCGACTCCATCATCCACAT; GGCCAATAATCCGTTCCAGG) were cloned into AAV vector under the expression of U6 and H1 promoters, respectively.

Stereotactic injections

Mice were prepared for stereotactic injections using standard procedures approved by the Stanford University Administrative Panel on Laboratory Animal Care. For anesthesia, the stock solution was made of dissolving 5 g of tribromoethanol into 5 ml of T-amyl alcohol and further diluted 80 folds into phosphate-buffered saline (PBS) to make the working solution. Working solution (0.2 ml; Avertin) per 10 g of body weight of mouse was used for anesthesia before mounting the mouse in the stereotax. The coordinates [AP (anterior-posterior); ML (medial-lateral); DV (dorsal-ventral) from Bregma] and volumes for the intercranial injections are as follows: (i) OB: +4.3/±0.85/−1.7 and + 5.3/±0.6/−1.5 with 1.0 μl of virus; and (ii) Piriform cortex: −0.7/±3.7/−4.75 with 0.75 μl of virus. The reference point on the DV axis for OB injection was on the surface of OB, while the reference point on the DV axis for piriform cortex injection was on the skull surface at AP/ML coordinate of −0.7/0.0.

Behavioral experiments

All behaviors were assessed in adult mice 2 to 3 months ago. Only male mice were used for the three-chamber sociability test.

Open field test

Mice were individually placed in a 40 cm–by–40 cm–by–40 cm white plastic chamber in a well-lit room and allowed to move freely for 10 min. Locomotor and exploratory behaviors were recorded using a Viewer III tracking system (Biobserve). Total distance traveled and time spent in the 20 cm–by–20 cm center of the square were quantified.

Three-chamber sociability test

A transparent three-chamber apparatus (60 cm by 30 cm by 30 cm per chamber) was used for sociability tests. For habituation, the subject was placed in the center chamber and allowed to explore the entire apparatus for 5 min. The peripheral chamber (left or right), in which the mouse spent more time was designated the preferred side. Subsequently, a stranger juvenile *Cbln1* cKO mouse was placed underneath an upside-down black wire-mesh cup within the nonpreferred chamber. The subject mouse was allowed to explore all three chambers freely for 10 min while being recorded using the Viewer III tracking system. Time spent in each chamber was quantified, and the sociability index was calculated by dividing the time spent in the stranger mouse-containing chamber by the time spent in the empty chamber.

Buried food-finding test

After 24 hours of food deprivation, the subject was placed in a new cage containing 3 cm of bedding, and 5 g of food pellet was buried in a random corner of the cage. The time it took for the mouse to dig up the food pellet was recorded.

Single-molecule in situ hybridization

Wild-type CD-1 mice were euthanized with isoflurane at P30 followed by transcardial perfusion with ice-cold PBS. Brains were quickly dissected and embedded in Optimal Cutting Temperature solution on dry ice. Sections with 12-μm thickness were sliced using a Leica cryostat 9CM3050-S) and mounted directly onto Superfrost Plus

histological slides. Single-molecule fluorescence in situ hybridization for Cbln1/2/4 mRNA (probe catalog nos. 538491-C2, 428551, and 300031-C3, respectively) was performed using the multiplex RNAscope platform [ACD (Advanced Cell Diagnostics)] according to manufacturer's instruction. Slides were mounted using ProLong Gold antifade mounting medium (Thermo Fisher Scientific, P36930) and imaged using Olympus VS120 slide scanner.

Immunohistochemistry

For synaptic marker staining, mice were anesthetized by avertin injection as described in stereotactic injection. Brains were extracted and postfixed in 4% PFA (Paraformaldehyde) for 1 hour. After postfixation, brains were washed three times with PBS and cryoprotected in 30% sucrose in PBS for 24 to 36 hours. Brains were sectioned coronally at 40 μm using a cryostat. For morphological tracing after electrophysiology, the slices were incubated in 4% PFA for 15 min. For immunostaining, the slices were blocked and permeabilized in 5% normal goat serum and 0.3% Triton X-100–containing PBS for 1 hour at room temperature. Primary antibodies against vGaT (SySy, 1:1000, RRID: AB_1106810), synaptophysin-2 (homemade with code Y941, 1:1000), MAP2 (Microtubule-associated protein 2) (Sigma-Aldrich, 1:1000, RRID: AB_477171), GFP (Thermo Fisher Scientific, 1:1000, RRID: AB_221569), or mCherry (Thermo Fisher Scientific, 1:1000, RRID: 2536611) were diluted in blocking buffer, and brain slices were incubated with primary antibody overnight at 4°C. For neurobiotin tracing, Streptavedin conjugated with Alexa Fluor 647 (Thermo Fisher Scientific, 1:1000) was included in the primary antibody mix. After three 10-min washes in PBS, slices were incubated with secondary antibodies: Alexa Fluor 488, Alexa Fluor 555, or Alexa Fluor 647. Slices underwent three 10-min washes in PBS and were mounted on positively charged glass slides, allowed to dry, and coverslipped.

Confocal microscopy

A Nikon A1RSi confocal microscope was used to acquire all images. Images are analyzed using Nikon analysis software. Within each set of experiments, the laser power, gain, offset, and pinhole size for each laser were kept constant. For quantification of synaptic puncta, *z*-stack images were obtained by at 0.5-μm intervals, and three slices (1 μm thickness in total) with highest signal were maximally projected. Automated background subtraction was performed using a rolling ball algorithm with a 1-μm radius. The same threshold was applied to each set of experiments, and puncta parameters were automatically obtained using the NIS-Elements. For quantification in the OB, the entire OB was sliced. Four sections with 400-μm anterior-posterior distance spacing were quantified, and each data point is an average of all slices quantified. The images were taken at either medial or lateral OB and were chosen randomly. All IHC (immunohistochemistry) data were collected and analyzed blindly.

Transmission EM

Three pairs of P28 *tBet-Cre/Cbln1* cKO mice and littermate controls without *tBet-Cre* allele were perfused with PBS followed by 4% PFA at 37°C. The brains were dissected out and postfixed in 2.5% glutaraldehyde and 2% paraformaldehyde in 0.1 M sodium cacodylate buffer (pH 7.4) overnight at 4°C. Coronal vibratome sections (200 μm) of the OB were collected in 0.1 M cold cacodylate buffer on the next day. The slices were subject to postfixation in 1% glutaraldehyde in 0.1 M cacodylate buffer before shipping to Yale CCMI (Center for Cellular and Molecular Imaging) EM facility. Slices were then postfixed in 1% OsO_4, 0.8% potassium ferricyanide in 0.1 M cacodylate buffer at room temperature for 1 hour. Specimens were then en bloc stained with 2% aqueous uranyl acetate for 45 min, dehydrated in a graded series of ethanol to 100%, substituted with propylene oxide and embedded in Embed 812 resin. Sample blocks were polymerized in an oven at 60°C overnight. Thin sections (60 nm) were cut by a Leica ultramicrotome (UC7) and poststained with 2% uranyl acetate and lead citrate. Sections were examined with a FEI Tecnai transmission electron microscope at 80 kV of accelerating voltage, and digital images were recorded with an Olympus Morada CCD camera and iTEM imaging software. Image analysis was performed using Fiji ImageJ. Excitatory synapses from mitral cells were identified by the presence of asymmetric membrane thickening and at least two presynaptic vesicles. Inhibitory synapses onto mitral cells were identified by the presence of symmetric membrane thickening and at least two presynaptic elliptical vesicles as compared to excitatory synapses. Synapse density were quantified by randomly sampling mitral cell dendrites, quantifying the number of synapses along the dendrites and normalizing the number by the total length of mitral cell dendrites analyzed in each mouse. Bouton size, the number of vesicles per bouton, the average vesicle size, vesicle ellipticity, and the average distance of vesicles to the active zone were quantified for inhibitory synapses onto mitral cells. All the parameters were averaged for each animal for statistical analysis. All EM data were acquired and analyzed blindly.

Junction-flanking PCR

A pair of primers (forward: 5′-CTGGCCAGTTATCGAACGCT-3′; reverse: 5′-GCGATGTTGGCATCGTTCTC-3′) annealing to constitutive exon sequences that flank SS4 exon were used to amplify *Nrxn123* mRNA transcripts with or without SS4. cDNA was first synthesized from equal amounts of immunoprecipitated mRNA from mitral/tufted cells and total input mRNA from the OB. Junction-flanking PCR was then performed with equal amount of cDNA from the two groups. The PCR products were separated on homemade MetaPhor agarose gel (Lonza) and stained with GelRed. Stained gel was imaged at subsaturation using the ChemiDoc Gel Imaging System (Bio-Rad). Quantification was performed using Image Lab (Bio-Rad) or ImageStudioLite (LI-COR). Intensity values were normalized to the size of DNA products to control for intensity differences caused by different dye incorporation owing to varied DNA length.

Surface binding assay and immunocytochemistry

Soluble recombinant HA-Cbln1-His and Nlgn1-ECD-Fc were first prepared as follows. FreeStyle HEK293F cells (Thermo Fisher Scientific) were transfected with plasmids expressing either HA-Cbln1-His or Nlgn1-ECD-Fc. The cell medium was collected 5 days after transfection. His-tagged Cbln1 were purified by Talon metal affinity resin (Clontech) and dialyzed against Hanks' balanced salt solution (HBSS). Fc-tagged Nlgn1-ECD were purified by rProteinA Sepharose Fast Flow (GE Healthcare), eluted with 10 mM glycine (pH 2.5), and dialyzed with HBSS. After obtaining soluble proteins, HEK293 cells were transfected with expression vectors for Flag-Nrxn1β with or without SS4. Vehicle, HA-Cbln1 (50 μg/ml), and Nlgn1-ECD-Fc (50 μg/ml) in HBSS with 2 mM $CaCl_2$ and 1 mM $MgCl_2$ were added to the transfected HEK293 cell sequentially with each

treatment lasting 1.5 hours at room temperature. After washing, the cells were fixed with 4% PFA and immunostained with mouse anti-HA (Covance, 1:1000, RRID: AB_2314672) or rabbit anti-Flag (Sigma-Aldrich, 1:1000, RRID: AB_439687), followed by incubation with Alexa Fluor 647–conjugated anti-human Fc γ and species-specific Alexa Fluor 488– or Alexa Fluor 546–conjugated secondary antibodies. Coverslips were mounted after three times of washing in PBS. Quantification was done by calculating the ratio of intensity of neurexin ligands' signals over Nrxn1β's signal on the HEK cell surface.

Cell aggregation assay

One batch of FreeStyle HEK293F cells was transfected with pCMV5-EGFP together with pCMV5-empty, pCMV5-Nrxn1β^{SS4-}, or pCMV5-Nrxn1β^{SS4-*} (with Nlgn binding mutations G155V and T156A). Another batch of FreeStyle HEK293F cells was transfected with pCMV5-mCherry together with pCMV5-empty and pCMV5 expression vectors containing Nlgn2 (pCMV5-Nlgn2). Cis co-expression of Nrxn1β and Nlgn2 was achieved by constructing plasmids coexpressing both using IRES (pCMV5-Nrxn1β^{SS4-}-IRES-Nlgn2, pCMV5-Nrxn1β^{SS4+-}-IRES-Nlgn2, pCMV5-Nrxn1β^{SS4-*-}-IRES-Nlgn2, and pCMV5-Nrxn1β^{SS4+*-}-IRES-Nlgn2). Cbln1 was coexpressed by the addition of a third plasmid pCMV5-Cbln1 during transfection. Forty-eight hours after transfection, 1 ml of HEK293F cells from each batch was mixed together in a 12-well Corning Costar Not Treated Plate (Millipore) and incubated at 37°C with shaking on Orbi-Shaker (Benchmark) with 125 rpm for 2 hours. Three images for each well were taken under confocal microscopy. Images were thresholded using Otsu's method, and Pearson's coefficient was calculated. Each data point represented averaged Pearson's coefficient for the three images taken for one round of experiments from transfection to imaging.

Statistical analysis

All experiments of electrophysiology, behavioral tests, immunohistochemistry analysis, EM, and cell culture experiments were performed and analyzed blindly to the experimental condition. Student's *t* test was used whenever the comparison is between two groups. The Kolmogorov-Smirnov test was used to analyze the cumulative curves. One-way analysis of variance (ANOVA) with Bonferroni's multiple hypothesis correction was used for comparison among more than two groups. Two-way ANOVA with Bonferroni's multiple hypothesis correction was used for comparison of multiple groups with multiple factors. The statistical test used for each experiment was specified in the figure legends. The "*n*" used for these analyses represents the number of mice for gene expression analysis, behavioral tests, immunohistochemistry analysis and EM analysis, the number of cells for electrophysiology and perisomatic synapse quantification, and the number of culture batches for surface binding assay and cell aggregation assay, all of which have been specified in the figure legends.

SUPPLEMENTARY MATERIALS

Supplementary material for this article is available at https://science.org/doi/10.1126/sciadv.abk1924

View/request a protocol for this paper from *Bio-protocol*.

REFERENCES AND NOTES

1. T. C. Südhof, The cell biology of synapse formation. *J. Cell Biol.* **220**, e202103052 (2021).
2. S. Jang, H. Lee, E. Kim, Synaptic adhesion molecules and excitatory synaptic transmission. *Curr. Opin. Neurobiol.* **45**, 45–50 (2017).
3. H. Y. Kim, J. W. Um, J. Ko, Proper synaptic adhesion signaling in the control of neural circuit architecture and brain function. *Prog. Neurobiol.* **200**, 101983 (2021).
4. A. Ribic, T. Biederer, H. Morishita, Emerging roles of synapse organizers in the regulation of critical periods. *Neural Plast.* **2019**, 1–9 (2019).
5. J. R. Sanes, S. L. Zipursky, Synaptic specificity, recognition molecules, and assembly of neural circuits. *Cell* **181**, 536–556 (2020).
6. T. C. Südhof, Synaptic neurexin complexes: A molecular code for the logic of neural circuits. *Cell* **171**, 745–769 (2017).
7. M. V. Fuccillo, C. H. Pak, Copy number variants in neurexin genes: Phenotypes and mechanisms. *Curr. Opin. Genet. Dev.* **68**, 64–70 (2021).
8. A. Tromp, B. Mowry, J. Giacomotto, Neurexins in autism and schizophrenia—A review of patient mutations, mouse models and potential future directions. *Mol. Psychiatry* **26**, 747–760 (2021).
9. E. Kasem, T. Kurihara, K. Tabuchi, Neurexins and neuropsychiatric disorders. *Neurosci. Res.* **127**, 53–60 (2018).
10. W. Rall, G. M. Shepherd, T. S. Reese, M. W. Brightman, Dendrodendritic synaptic pathway for inhibition in the olfactory bulb. *Exp. Neurol.* **14**, 44–56 (1966).
11. F. Ango, N. B. Gallo, L. Van Aelst, Molecular mechanisms of axo-axonic innervation. *Curr. Opin. Neurobiol.* **69**, 105–112 (2021).
12. K. K. Cover, B. N. Mathur, Axo-axonic synapses: Diversity in neural circuit function. *J. Comp. Neurol.* **1**, 2391–2401 (2020).
13. G. M. Shepherd, W. R. Chen, C. A. Greer, in *The Synaptic Organization of the Brain*, G. M. Shepherd, Ed. (Oxford Univ. Press, New York, 2004), pp. 165–216.
14. N. N. Urban, A. C. Arevian, Computing with dendrodendritic synapses in the olfactory bulb. *Ann. N. Y. Acad. Sci.* **1170**, 264–269 (2009).
15. G. M. Shepherd, M. L. Hines, M. Migliore, W. R. Chen, C. A. Greer, Predicting brain organization with a computational model: 50-year perspective on lateral inhibition and oscillatory gating by dendrodendritic synapses. *J. Neurophysiol.* **124**, 375–387 (2020).
16. Z. Liu, Z. Chen, C. Shang, F. Yan, Y. Shi, J. Zhang, B. Qu, H. Han, Y. Wang, D. Li, T. C. Südhof, P. Cao, IGF1-dependent synaptic plasticity of mitral cells in olfactory memory during social learning. *Neuron* **95**, 106–122.e5 (2017).
17. E. V. Famiglietti, Dendro-dendritic synapses in the lateral geniculate nucleus of the cat. *Brain Res.* **20**, 181–191 (1970).
18. B. N. Harding, Dendro-dendritic synapses, including reciprocal synapses, in the ventrolateral nucleus of the monkey thalamus. *Brain Res.* **34**, 181–185 (1971).
19. J. J. Sloper, T. P. Powell, Dendro-dendritic and reciprocal synapses in the primate motor cortex. *Proc. R. Soc. Lond. Ser. B Biol. Sci.* **203**, 23–38 (1978).
20. E. Hartveit, Reciprocal synaptic interactions between rod bipolar cells and amacrine cells in the rat retina. *J. Neurophysiol.* **81**, 2923–2936 (1999).
21. T. J. Siddiqui, A. M. Craig, Synaptic organizing complexes. *Curr. Opin. Neurobiol.* **21**, 132–143 (2011).
22. M. Yuzaki, A. R. Aricescu, A GluD Coming-Of-Age Story. *Trends Neurosci.* **40**, 138–150 (2017).
23. M. Yuzaki, Two classes of secreted synaptic organizers in the central nervous system. *Annu. Rev. Physiol.* **80**, 243–262 (2018).
24. Y. A. Ushkaryov, A. G. Petrenko, M. Geppert, T. C. Südhof, Neurexins: Synaptic cell surface proteins related to the α-latrotoxin receptor and laminin. *Science* **257**, 50–56 (1992).
25. Y. A. Ushkaryov, T. C. Südhof, Neurexin III alpha: Extensive alternative splicing generates membrane-bound and soluble forms. *Proc. Natl. Acad. Sci. U.S.A.* **90**, 6410–6414 (1993).
26. K. Tabuchi, T. C. Südhof, Structure and evolution of neurexin genes: Insight into the mechanism of alternative splicing. *Genomics* **79**, 849–859 (2002).
27. F. H. Sterky, J. H. Trotter, S. Lee, C. V. Recktenwald, X. Du, B. Zhou, P. Zhou, J. Schwenk, B. Fakler, T. C. Südhof, Carbonic anhydrase-related protein CA10 is an evolutionarily conserved pan-neurexin ligand. *Proc. Natl. Acad. Sci. U.S.A.* **114**, E1253–E1262 (2017).
28. B. Ullrich, Y. A. Ushkaryov, T. C. Südhof, Cartography of neurexins: More than 1000 isoforms generated by alternative splicing and expressed in distinct subsets of neurons. *Neuron* **14**, 497–507 (1995).
29. M. Uchigashima, A. Cheung, J. Suh, M. Watanabe, K. Futai, Differential expression of neurexin genes in the mouse brain. *J. Comp. Neurol.* **527**, 1940–1965 (2019).
30. R. Haddad, A. Lanjuin, L. Madisen, H. Zeng, V. N. Murthy, N. Uchida, Olfactory cortical neurons read out a relative time code in the olfactory bulb. *Nat. Neurosci.* **16**, 949–957 (2013).
31. L. Madisen, T. A. Zwingman, S. M. Sunkin, S. W. Oh, H. A. Zariwala, H. Gu, L. L. Ng, R. D. Palmiter, M. J. Hawrylycz, A. R. Jones, E. S. Lein, H. Zeng, A robust and high-throughput Cre reporting and characterization system for the whole mouse brain. *Nat. Neurosci.* **13**, 133–140 (2010).
32. E. Sanz, L. Yang, T. Su, D. R. Morris, G. S. McKnight, P. S. Amieux, Cell-type-specific isolation of ribosome-associated mRNA from complex tissues. *Proc. Natl. Acad. Sci. U.S.A.* **106**, 13939–13944 (2009).
33. Z. Pang, J. Zuo, J. I. Morgan, Cbln3, a novel member of the precerebellin family that binds specifically to Cbln1. *J. Neurosci.* **20**, 6333–6339 (2000).
34. E. Seigneur, T. C. Südhof, Genetic ablation of all cerebellins reveals synapse organizer functions in multiple regions throughout the brain. *J. Neurosci.* **38**, 4774–4790 (2018).

35. K. Matsuda, E. Miura, T. Miyazaki, W. Kakegawa, K. Emi, S. Narumi, Y. Fukazawa, A. Ito-Ishida, T. Kondo, R. Shigemoto, M. Watanabe, M. Yuzaki, Cbln1 is a ligand for an orphan glutamate receptor d2, a bidirectional synapse organizer. *Science* **338**, 1541–1545 (2010).
36. T. Uemura, S. J. Lee, M. Yasumura, T. Takeuchi, T. Yoshida, M. Ra, R. Taguchi, K. Sakimura, M. Mishina, Trans-synaptic interaction of GluRδ2 and Neurexin through Cbln1 mediates synapse formation in the cerebellum. *Cell* **141**, 1068–1079 (2010).
37. A. Ito-Ishida, T. Miyazaki, E. Miura, K. Matsuda, M. Watanabe, M. Yuzaki, S. Okabe, Presynaptically released Cbln1 induces dynamic axonal structural changes by interacting with GluD2 during cerebellar synapse formation. *Neuron* **76**, 549–564 (2012).
38. A. Ito-Ishida, W. Kakegawa, K. Kohda, E. Miura, S. Okabe, M. Yuzaki, Cbln1 downregulates the formation and function of inhibitory synapses in mouse cerebellar Purkinje cells. *Eur. J. Neurosci.* **39**, 1268–1280 (2014).
39. K. Ibata, M. Kono, S. Narumi, J. Motohashi, W. Kakegawa, K. Kohda, M. Yuzaki, Activity-dependent secretion of synaptic organizer cbln1 from lysosomes in granule cell axons. *Neuron* **102**, 1184–1198.e10 (2019).
40. J. Dai, C. Patzke, K. Liakath-Ali, E. Seigneur, T. C. Südhof, GluD1 is a signal transduction device disguised as an ionotropic receptor. *Nature* **595**, 261–265 (2021).
41. E. Seigneur, J. Wang, J. Dai, J. Polepalli, T. C. Südhof, Cerebellin-2 regulates a serotonergic dorsal raphe circuit that controls compulsive behaviors. *Mol. Psychiatry*, 1–13 (2021).
42. M. D. Eyre, M. Antal, Z. Nusser, Distinct deep short-axon cell subtypes of the main olfactory bulb provide novel intrabulbar and extrabulbar gabaergic connections. *J. Neurosci.* **28**, 8217–8229 (2008).
43. F. W. Zhou, Z. Y. Shao, M. T. Shipley, A. C. Puche, Short-term plasticity in glomerular inhibitory circuits shapes olfactory bulb output. *J. Neurophysiol.* **123**, 1120–1132 (2020).
44. H. Hirai, Z. Pang, D. Bao, T. Miyazaki, L. Li, E. Miura, J. Parris, Y. Rong, M. Watanabe, M. Yuzaki, J. I. Morgan, Cbln1 is essential for synaptic integrity and plasticity in the cerebellum. *Nat. Neurosci.* **8**, 1534–1541 (2005).
45. M. Bergmann, T. Schuster, D. Grabs, B. Marquèze-Pouey, H. Betz, H. Traurig, A. Mayerhofer, M. Gratzl, Synaptophysin and synaptoporin expression in the developing rat olfactory system. *Dev. Brain Res.* **74**, 235–244 (1993).
46. H. Naritsuka, K. Sakai, T. Hashikawa, K. Mori, M. Yamaguchi, Perisomatic-targeting granule cells in the mouse. *J. Comp. Neurol.* **426**, 409–426 (2009).
47. F. Varoqueaux, S. Jamain, N. Brose, Neuroligin 2 is exclusively localized to inhibitory synapses. *Eur. J. Cell Biol.* **83**, 449–456 (2004).
48. K. Ichtchenko, Y. Hata, T. Nguyen, B. Ullrich, M. Missler, C. Moomaw, T. C. Südhof, Neuroligin 1: A splice site-specific ligand for β-neurexins. *Cell* **81**, 435–443 (1995).
49. K. Ichtchenko, T. Nguyen, T. C. Südhof, Structures, alternative splicing, and neurexin binding of multiple neuroligins. *J. Biol. Chem.* **271**, 2676–2682 (1996).
50. T. Nguyen, T. C. Südhof, Binding properties of neuroligin 1 and neurexin 1β reveal function as heterophilic cell adhesion molecules. *J. Biol. Chem.* **272**, 26032–26039 (1997).
51. M. F. Bolliger, J. Pei, S. Maxeiner, A. A. Boucard, N. V. Grishin, T. C. Südhof, Unusually rapid evolution of Neuroligin-4 in mice. *Proc. Natl. Acad. Sci. U.S.A.* **105**, 6421–6426 (2008).
52. S. Chanda, W. D. Hale, B. Zhang, M. Wernig, T. C. Südhof, Unique versus redundant functions of neuroligin genes in shaping excitatory and inhibitory synapse properties. *J. Neurosci.* **37**, 6816–6836 (2017).
53. B. Zhang, L. Y. Chen, X. Liu, S. Maxeiner, S. J. Lee, O. Gokce, T. C. Südhof, Neuroligins sculpt cerebellar purkinje-cell circuits by differential control of distinct classes of synapses. *Neuron* **87**, 781–796 (2015).
54. B. Zhang, T. C. Südhof, Neuroligins are selectively essential for NMDAR signaling in cerebellar stellate interneurons. *J. Neurosci.* **36**, 9070–9083 (2016).
55. B. Zhang, O. Gokce, W. D. Hale, N. Brose, T. C. Südhof, Autism-associated neuroligin-4 mutation selectively impairs glycinergic synaptic transmission in mouse brainstem synapses. *J. Exp. Med.* **215**, 1543–1553 (2018).
56. D. G. R. Tervo, B.-Y. Hwang, S. Viswanathan, T. Gaj, M. Lavzin, K. Ritola, S. Lindo, S. Michael, E. Kuleshova, D. Ojala, C.-C. Huang, C. R. Gerfen, J. Schiller, J. T. Dudman, A. W. Hantman, L. L. Looger, D. V. Schaffer, A. Y. Karpova, A designer AAV variant permits efficient retrograde access to projection neurons. *Neuron* **92**, 372–382 (2016).
57. J. Y. Joo, S. J. Lee, T. Uemura, T. Yoshida, M. Yasumura, M. Watanabe, M. Mishina, Differential interactions of cerebellin precursor protein (Cbln) subtypes and neurexin variants for synapse formation of cortical neurons. *Biochem. Biophys. Res. Commun.* **406**, 627–632 (2011).
58. K. Matsuda, M. Yuzaki, Cbln family proteins promote synapse formation by regulating distinct neurexin signaling pathways in various brain regions. *Eur. J. Neurosci.* **33**, 1447–1461 (2011).
59. J. Dai, J. Aoto, T. C. Südhof, Alternative splicing of presynaptic neurexins differentially controls postsynaptic NMDA and AMPA receptor responses. *Neuron* **102**, 993–1008.e5 (2019).
60. M. Yasumura, T. Yoshida, S. J. Lee, T. Uemura, J. Y. Joo, M. Mishina, Glutamate receptor δ1 induces preferentially inhibitory presynaptic differentiation of cortical neurons by interacting with neurexins through cerebellin precursor protein subtypes. *J. Neurochem.* **121**, 705–716 (2012).
61. D. Araç, A. A. Boucard, E. Özkan, P. Strop, E. Newell, T. C. Südhof, A. T. Brunger, Structures of Neuroligin-1 and the Neuroligin-1/Neurexin-1β Complex Reveal Specific Protein-Protein and Protein-Ca2+ Interactions. *Neuron* **56**, 992–1003 (2007).
62. X. Chen, H. Liu, A. H. R. Shim, P. J. Focia, X. He, Structural basis for synaptic adhesion mediated by neuroligin-neurexin interactions. *Nat. Struct. Mol. Biol.* **15**, 50–56 (2008).
63. C. Reissner, M. Klose, R. Fairless, M. Missler, Mutational analysis of the neurexin/neuroligin complex reveals essential and regulatory components. *Proc. Natl. Acad. Sci. U.S.A.* **105**, 15124–15129 (2008).
64. L. Y. Chen, M. Jiang, B. Zhang, O. Gokce, T. C. Südhof, Conditional deletion of all neurexins defines diversity of essential synaptic organizer functions for neurexins. *Neuron* **94**, 611–625.e4 (2017).
65. R. J. Platt, S. Chen, Y. Zhou, M. J. Yim, L. Swiech, H. R. Kempton, J. E. Dahlman, O. Parnas, T. M. Eisenhaure, M. Jovanovic, D. B. Graham, S. Jhunjhunwala, M. Heidenreich, R. J. Xavier, R. Langer, D. G. Anderson, N. Hacohen, A. Regev, G. Feng, P. A. Sharp, F. Zhang, CRISPR-Cas9 knockin mice for genome editing and cancer modeling. *Cell* **159**, 440–455 (2014).
66. J. H. Trotter, Z. Dargaei, A. Sclip, S. Essayan-Perez, K. Liakath-Ali, K. Raju, A. Nabet, X. Liu, T. C. Südhof, Compartment-specific neurexin nanodomains orchestrate tripartite synapse assembly. *bioRxiv* 2020.08.21.262097 (2021).

Acknowledgment

Funding: Stanford Interdisciplinary Graduate Fellowship (C.Y.W.), National Institutes of Health (NIH) KO1 MH105040-01 and BBRF Young Investigator Grant (J.H.T.), European Molecular Biology Organization Long Term Fellowship (ALTF 803-2017) and Larry L. Hillblom Foundation Fellowship grant (2020-A-016-FEL) (K.L.-A.), and National Institutes of Mental Health grant MH052804 (T.C.S.). **Author contributions:** C.Y.W. and T.C.S. conceived this study and wrote the manuscript with input from the other authors. With guidance from T.C.S., C.Y.W. designed and conducted all experiments except RiboTag RNA profiling (by J.H.T.), single-molecule in situ hybridization (by K.L.-A.), cell surface binding assay (by S.-J.L.), and EM image acquisition (by X.L.). C.Y.W. performed data analyses. All authors reviewed and approved the final manuscript. **Competing interests:** The authors declare that they have no conflict of interest. **Data and materials availability:** All data needed to evaluate the conclusions in the paper are present in the paper and/or the Supplementary Materials. All reagents generated in this study are available upon reasonable requests to the lead contact T.C.S.

Submitted 28 June 2021
Accepted 1 November 2021
Published 17 December 2021
10.1126/sciadv.abk1924